

DISCLAIMER:

This document does not meet the
current format guidelines of
the Graduate School at
The University of Texas at Austin.

It has been published for
informational use only.

Copyright
by
Wentao Wang
2019

The Thesis Committee for Wentao Wang

Certifies that this is the approved version of the following thesis:

**Three-Dimensional Geological Modelling of the Lithofacies of Caddo
Limestone in Stephens County, North-Central Texas**

**APPROVED BY
SUPERVISING COMMITTEE:**

Supervisor:	Xavier Janson
Co-Supervisor:	Qilong Fu
	Scott W. Tinker
	Timothy M. Shanahan

**Three-Dimensional Geological Modelling of the Caddo Limestone
Mounds in Stephens County, North-Central Texas**

by

Wentao Wang

Thesis

Presented to the Faculty of the Graduate School of
The University of Texas at Austin
in Partial Fulfilment
of the Requirements
for the Degree of

Master of Science in Geological Sciences

The University of Texas at Austin

May 2019

Dedication

To my parents and friends, either in China or in the USA.

Acknowledgements

First, I would like to express my gratitude to my supervisors, Dr. Xavier Janson and Dr. Qilong Fu, for their continuing instructions, suggestions and support throughout my study at The University of Texas at Austin. Dr. Qilong Fu spent much time instructing me on my research project and helping me to consolidate my geologic foundation. Special thanks go to Dr. Xavier Janson, who convened weekly meetings, in which I was asked many challenging questions, which, in turn, enhanced my critical thinking and cultivated my ability to solve problems. I also thank the PI of my research project, William A. Ambrose, for his help during my stay at the Bureau of Economic Geology, and thank the State of Texas Advanced Resources Recovery (STARR) group for funding my research study. BASA Resources, Inc., provided seismic volumes and some petrophysical data. Moreover, I thank my two other committee members, Dr. Scott W. Tinker and Dr. Timothy M. Shanahan, for their guidance and interesting courses.

I also want to express my gratitude to the researchers and staffs at the Bureau of Economic Geology (BEG) and University of Texas Institute for Geophysics (UTIG). Transferring from an Electronic Engineering major to Geosciences was not an easy process and they helped me greatly. I thank Dallas B. Dunlap and Dr. Osareni C. Ogiesoba for their help in getting the 3-D seismic data for my research project, especially for Dallas Dunlap's instructions on DecisionSpace. I thank Mr. Thomas Hess for coaching me on seismic processing. Additionally, I would like to say thank you to the BEG Core Research Center staff, especially Nathan Ivicic and Brandon Williamson. They spent a lot of time and effort helping me prepare the cores needed and collect the core data. In addition, my thanks go to Joseph Yeh and Carlos Chuck Garza for their help with my software.

Thanks to my colleagues: Liu Li, Peng Junwen, and Vinyet Baques, for listening to my presentation before Master's Tuesday and providing me with valuable comments. Thanks to my friends and classmates: Chen Jiabin, Henar Rebadan, Javier Jasso, Jiang Yile, Liang Zexi, Qi Rui, Shen Yanyao, Wang Yinuo, Wang Yining, Wu Xiaohan, Zhu Wenjie, for their endless encouragement, especially in my last semester.

Most of all, I would like to thank my parents, who are excellent geologists and geophysicists, for their endless love and support, which inspired and encouraged me to be devoted to the energy industry.

Abstract

Three-Dimensional Geological Modelling of the Caddo Limestone Mounds in Stephens County, North-Central Texas

Wentao Wang, M.S. Geo. Sci.

The University of Texas at Austin, 2019

Co-Supervisors: Xavier Janson, Qilong Fu

The Pennsylvanian (early Desmoinesian) Caddo Limestone in Stephens County, Texas hosts important reservoirs and hydrocarbon resources. Therefore, constructing a three-dimensional geological model of the Caddo Limestone is of great significance.

The Caddo Limestone Formation comprises shelf carbonate build-ups in which the major allochems are phylloid algal and *Komia*. This study focuses on the uppermost two cycles of the Caddo Limestone. This study integrated geological, geophysical and petrophysical analysis to build a three-dimensional geological model of the Caddo Limestone. The model is based on 18 cores (totalling 700 ft long), wireline logs from 173 wells and 3-dimensional seismic data.

A 3D structure model derived from 3D seismic data and 3D geocellular model of lithofacies are the two key products of this study. Five lithofacies have been differentiated: (1) *Komia* wackestone and mud-dominated packstone, (2) Phylloid-algal wackestone and packstone, (3) Bioclastic wackestone to packstone, (4) *Komia* grainstone and grain-dominated packstone, and (5) *Komia* boundstone. An artificial Neural Network (ANN) algorithm was applied to predict

lithofacies in wells without core samples. The lithofacies were extrapolated within the geocellular model using indicator Kriging. This work demonstrated a viable workflow to build 3D reservoir models of Paleozoic carbonate mound reservoirs.

Contents

List of Tables	xi
List of Figures	xii
Introduction	1
Location of the Study Area.....	2
Previous Work	2
Research Objectives	6
Geological Setting.....	8
Regional Setting.....	8
Local Stratigraphy.....	10
Methodologies and Dataset	12
Petrographic Observation	13
Core study.....	13
Thin sections.....	15
Wireline logs.....	15
Three-dimensional seismic data.....	15
Lithofacies	17
Structure Map	17
Lithofacies Descriptions	23
<i>Komia</i> grain-dominated packstone and grainstone	25
<i>Komia</i> boundstone.....	30
Phylloid-algal wackestone and packstone	32
Bioclast wackestone to packstone.....	37

Depositional-Environmental Interpretation	40
Geological Modelling.....	44
Well Log and Artificial Neural Network.....	44
Well Correlation by Cores	47
Lithofacies Distribution Map.....	51
Statistical and Component Analysis.....	61
Discussion.....	67
Conclusion	71
References	73
Vita.....	73

List of Tables

Table 1: Cored wells in Stephens County, North-Central Texas.....	14
Table 2: Major lithofacies and interpreted depositional environments at the Caddo Limestone in Stephens County North-Central Texas.	41
Table 3: Proportion of five lithofacies types in Cycle-A, acquired from <i>Petrel</i>	63
Table 4: Proportion of five lithofacies types in Cycle-B, acquired from <i>Petrel</i>	63
Table 5: Composite footage of five lithofacies types in Cycle A, acquired from core samples...	65

List of Figures

Figure 1: Map of the Eliasville Oil Field study area in Stephens County, north-Central Texas (from Fu et al., 2017).	2
Figure 2: Paleogeographic map of the Desmoinesian showing structural elements and depositional systems in North-Central and West-Central Texas. Rectangle in the central of diagram indicates location of Stephens County. Cities: Ab = Abilene; Br = Brownwood; DL = Dallas; FW = Fort Worth; SA = San Angelo. Red indicates the boundary between the Concho Platform and the Fort Worth Basin. Modified after Fu et al., (2017), based on Yancey and Cleaves (1990) and Cleaves (2000).	8
Figure 3: (A) Geologic timeline showing the 1st-order curve with respect to present-day sea level, the rate of production of ocean crust and the condition of glaciation. After Plint et al., 1992. (B) Plot of relative change in eustasy for the late Pennsylvanian, blue curve shows the 2nd-order and red curve shows the 3rd-order, indicating the sea-level variation in the early Desmoinesian with the red arrow, modified after Ross and Ross, 1987 and Wright, 2011.	9
Figure 4: Stratigraphic chart of Mississippian and Pennsylvanian formations in Stephens County, North-Central Texas, from Fu et al., 2017, modified from Cheney and Gross, 1952; Brown, 1973; Weber, 1995; Pollastro et al., 2007.	11
Figure 5: Flow chart of the study involving 3-D seismic data, geologic data and petrophysical data	13

Figure 6: Map of Eliasville and East Eliasville fields. The red boundary shows the Eliasville field, and the green boundary shows the East Eliasville field. The red line and the green line represent cross sections I and II, respectively. 18

Figure 7: Stratigraphic cross section I showing the Cycle A and Cycle B in the Caddo Limestone based on wireline logs (GR and RHOB) calibrated by cores. See Figure 4-1 for location of the cross section. 19

Figure 8: Stratigraphic cross section showing Cycle A and Cycle B in the Caddo Limestone based on wireline logs (GR and RHOB) calibrated by cores. See Figure 4-1 for location of the cross section. 20

Figure 9: 3-D structure map on the top of the Caddo Limestone constructed from the seismic data in the study area, in which the alignment direction of carbonate mounds and the topographic highs are shown.....21

Figure 10: (A) 2-D structure map constructed from the seismic data and wireline log data in the study area. (B) Isochore map of Cycle A interval at the Caddo Limestone showing variations in thickness from about 10 to 65 ft, established with 173 wells shown on the map. (B) Isochore map of Cycle B interval at the Caddo Limestone showing variations in thickness from approximately 0 to 40 ft, established with 173 wells shown on the map.22

Figure 11: Diagrams of *Komia* (From Flügel, 2010) (A) Schematics of *Komia* showing its internal structure. (B) Photomicrographs of *Komia* from the East Eliasville Caddo Unit #WI-115 well, 3367.9 ft.....24

Figure 12: Microphotographs of *Komia* lithofacies. (A) Microphotograph showing *Komia* wackestone and mud-dominated packstone, *Komia* is indicated by the red arrows. (B)

Microphotograph showing *Komia* (red arrow) the calcite cement infilling an intragranular pore resulted from dissolution, as is enclosed by the rectangle. (C) Microphotograph showing the stalk of *Komia* in the vertical cut surface. (D) Microphotograph showing *Komia* fragments that are diagenetically altered. (E) Microphotograph showing lithofacies of *Komia* wackstone, courtesy of Qilong Fu. (F) Microphotograph showing *Komia* wackstone with intergranular pores generated by diagenesis, courtesy of Qilong Fu.25

Figure 13: (A) Photomicrograph showing bryozoans, from the Newell, Dell #2 well, 3383.81 ft. (B) An enlarged version of Figure (A) showing the detailed structure of bryozoans spines, the dissolution of calcite, and micropores as well as macropores.27

Figure 14: (A) Photomicrograph showing miliolid (solid red arrow) and cemented vugs formed through dissolution and recrystallization (hollow arrow), from the Newell, Dell #2 well, 3394.9 ft. (B) Photomicrograph demonstrating a completely cement-filled miliolid (solid red arrow), in which there are micropores generated (hollow arrow), from the Newell Dell #2 well, 3367.9 ft. (C) Photomicrograph showing a fusulinid with intragranular pores present and its matrix completely dissolved, through which more macropores were generated. (D) Photomicrograph demonstrating a fusulinid - in which intragranular pores are completely occluded. Thin section was stained with Alizarin Red-S solution.....28

Figure 15: (A) Photomicrograph of *Komia* wackstone and packstone with interparticle pores, from the Newell Dell #2 well, 3297.8 ft, courtesy of Qilong Fu. (B) Photomicrograph of *Komia* wackstone where most of the *Komia* are diagenetically altered, from the Newell Dell #2 well, 3289.5 ft. (C) Photomicrograph of *Komia* packstone with vuggy

pores, from the Newell Dell #2 well, 3281.6 ft. (D) Photomicrograph of *Komia* wackestone showing cracks and channels, from the Newell Dell #2 well, 3274.0 ft, courtesy of Qilong Fu.29

Figure 16: (A) Photomicrograph of *Komia* fusulinid grainstone where *Komia* is indicated by the yellow arrow. Calcite is stained with Alizarin Red-S solution. (B) Photomicrograph of *Komia* grain-dominated packstone with *Komia* indicated by the red arrow. (C) Photomicrograph of *Komia* grainstone. Calcite is stained with Alizarin Red-S solution, from the Newell Dell #2 well, 3222.2 ft. (D) Photomicrograph of *Komia* grain-dominated packstone, from the Eliasville Caddo Unit #106 well, 3261.6 ft. 30

Figure 17: (A) Photomicrograph of *Komia* boundstone with red arrows indicating the growth direction of *Komia* thallus, from the Kirkland I.E. #A6 well, 3375.6 ft. (B) Photomicrograph of *Komia* boundstone showing intergrain and intragrain porosity, from the Newell Dell #2 well, 3270.3 ft.32

Figure 18: (A) Kirkland I.E. #A6 well, core sample of *Komia* boundstone, *Komia* in situ growth. (B) Eliasville #106 well, 3242.8 to 3243.4 ft. (C) Eliasville #106 well, 3256.5 ft, core sample of *Komia* boundstone, courtesy of Qilong Fu.33

Figure 19: (A) Photomicrograph showing phylloid-algal wackestone, where the phylloid-algal blades have gone through extensive diagenesis, from the Newell Dell #2 well. (B) Photomicrograph demonstrating phylloid-algal wackestone and mud-dominated packstone with a well-developed porosity system within the blades, where micro- and macro-pores were generated through diagenesis, from the Newell Dell #2 well. Photomicrographs courtesy of Qilong Fu.35

Figure 20: (A) Phylloid-algal wackestone with phylloid algal fragments in the rectangle and stylolite (arrow). Eliasville Caddo Unit #33, 3244.1 ft - 3244.6 ft. (B) Phylloid-algal wackestone showing large sinuous phylloid-algal blades on the surface. Ward #97, 3170.2 - 3170.5 ft. Photos courtesy of Qilong Fu, 19th September, 2016.36

Figure 21: Photomicrographs of bioclast wackestone and packstone. Thin sections were stained with Alizarin Red-S solution. (A) & (B) Sparitic microbial bioclast wackestone that was recrystallized, where major bioclasts are *Komia*, bryozoans, and brachiopods, from the New Dell #2 well. (C) Bioclast wackestone with fragments of bryozoans and *Komia*. (D) Bioclast wackestone from the Eliasville Caddo Unit #106 well, 3273.3 ft. (E) Slightly dolomitic bioclast wackestone from the Eliasville Caddo Unit #106 well, 3259.1 ft. (F) Bioclast wackestone with *Komia* and crinoid, from the Eliasville #106 well, 3259.1 ft. Only the upper half was stained with Alizarin Red-S solution. Photomicrograph courtesy of Qilong Fu. (G) Bioclast packstone showing fragments of bryozoans, *Komia* and crinoids, from the Newell Dell #2 well, 3281.8 ft. (H) Bioclast packstone showing the fragments of *Komia* and fusulinids, from the Newell Dell #2 well, 3289.5 ft.39

Figure 22: Simplified conceptual diagram of a backpropagation artificial neural network.....45

Figure 23: An integrated ANN system with multiple inputs and various layers.....46

Figure 24: An artificial neural network in which the input is the data from two wells and the output is the predicted lithofacies distribution on these two wells47

Figure 25: Well correlation and lithofacies simulation, Eliasville Caddo Unit #33 and East Eliasville Caddo Unit #46.....49

Figure 26: Lithofacies distribution of the Eliasville Caddo #86 well, from both core description (L86-A) and the artificial neural network’s simulation (L86-B).50

Figure 27: Lithofacies distribution of the Eliasville Caddo #131 well, from both core description (L131-A) and the artificial neural network’s simulation (L131-B).....51

Figure 28: 3-D Lithofacies distribution map of Cycle-A. *Komia* grainstone and grain-dominated packstone are indicated in blue, Phylloid-algal wackestone and packstone are indicated in yellow, *Komia* wackestone and mud-dominated packstone are indicated by green, *Komia* boundstone is indicated in indigo, and the bioclast wackestone is indicated in pinkish red and the lime mud/shale is in gray.....533

Figure 29: Fence diagram of Cycle A showing lithofacies distribution within the architecture, with an enlarged diagram of Figure 1-5 displaying phylloid-algal wackestone and packstone.544

Figure 30: Ten surfaces sampled from the 3-D facies map of Cycle A showing the vertical variation of lithofacies distribution with respect to the Z-axis.566

Figure 31: A 3-dimensional lithofacies model of Cycle A with the Z scale set as 50. Red line of dashes indicates the thickness trend from the non-mound region to mounds.....57

Figure 32: A 3-D lithofacies distribution map of Cycle B. *Komia* grainstone and grain-dominated packstone are indicated in blue, Phylloid-algal wackestone and packstone are indicated in yellow, *Komia* wackestone and mud-dominated packstone are indicated in green, *Komia* boundstone is indicated in indigo, the bioclast wackestone is indicated in pinkish-red while the lime mud/shale is represented gray.....599

Figure 33: Fence diagram of Cycle B showing lithofacies distribution.....60

Figure 34: Eight surfaces sampled from the 3-D facies map of Cycle B, showing the vertical variation of lithofacies distribution with respect to the Z-axis.61

Figure 35. Estimated facies proportions and vertical distribution for both Cycle A and Cycle B64

Figure 36. Facies proportions of Cycle A, KP/G = *Komia* grain-dominated packstone and grainstone, PP/W = Phylloid-algal wackestone and packstone, KP/W = *Komia* wackestone and mud-dominated packstone, KB = *Komia* boundstone and BW = Bioclast wackestone. The M columns represent facies proportions of the model, the C columns represent facies proportions of the core samples and the L columns represent facies proportions from the well logs.....66

Figure 37. (A) Depositional model of Caddo mound complexes showing a *Komia* flat formed above fair-weather wave base at the top of a phylloid algal mound, after Fu & Loucks, 2017. (B) Cross section of two carbonate mounds showing the vertical distribution of lithofacies at Cycle A.....69

Introduction

The Fort Worth Basin of North-Central Texas and southwestern Oklahoma is a significant hydrocarbon-producing province in the United States. The Caddo Limestone is one of the hydrocarbon-bearing strata in the basin. Lewis (1987) modelled the structure of the Caddo Limestone, and Forehand (1991) further characterized the Caddo algal mounds. Loucks and Fu (2016) focused on the Caddo shelf-buildup complexes and studied their lithofacies tied to porosity and permeability to different facies.

While most researchers focus on qualitative analysis of the Caddo Limestone, there are no previous work conducted on modelling the Caddo Limestone reservoir in three dimension. Constructing a three-dimensional model of the lithofacies of the Caddo allows better predictions of the total hydrocarbon reserves and will help future production forecasts and development. This study investigates how to realistically distribute the lithofacies within the Caddo Limestone in a three-dimensional geocellular model using artificial neural network analysis and geostatistical spatial distribution.

This thesis demonstrates a simple workflow that integrates 3D seismic interpretation, core and well-log correlation, geo-statistical analysis and lithofacies 3D modelling. The geological validation of the 3D model is performed by comparing an existing conceptual facies model of Caddo Limestone and the constructed 3D geocellular model. Comparison of the study's workflow with other studies that model carbonate mounds in 3D could result in improved geological accuracy.

Location of the Study Area

The study area is located in Stephens County, Texas. There are four oil fields in the area, and the Eliasville Oil Field is the focus of this study.

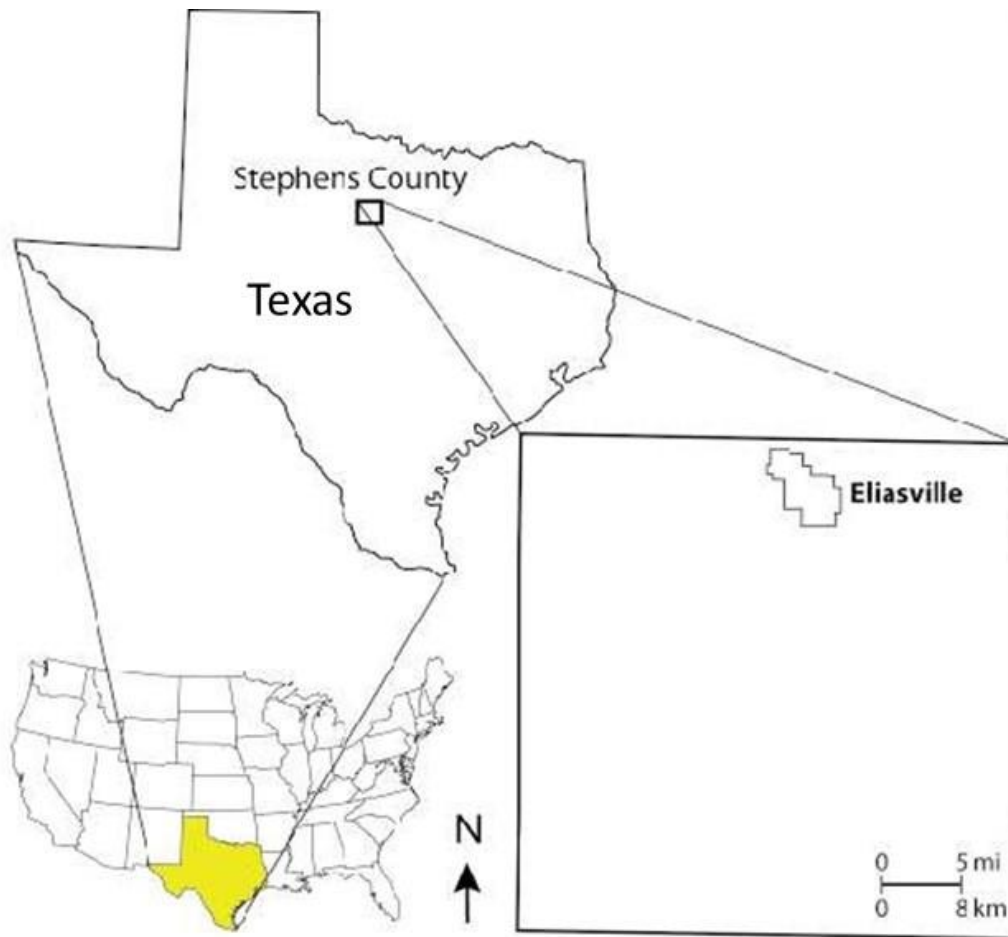


Figure 1: Map of the study area (Eliasville Oil Field) in Stephens County, North-Central Texas (Modified from Fu et al., 2017).

Previous Work

Early work conducted on the algal mounds dates from 1969, when Philip Heckel studied phylloid mound complexes in the Upper Pennsylvanian rocks of the Mid-Continent in outcrops.

Heckel (1974) researched Desmoinesian algal mounds, algal mounds were much better developed and more widespread in the Desmoinesian than during the Atokan.

With production activity progressing in the Fort Worth Basin, more attention was paid to the Caddo Limestone, and a few studies of the Caddo algal mounds have been published. Crabtree (1987) conducted an extensive analysis of reservoir characteristics of the Caddo Limestone at Stephens County. Lewis (1987) provided a detailed structural model for the Caddo Limestone on the Concho Platform in the western part of Stephens County. Forehand (1991) conducted a characterization of Caddo algal mounds and documented three major parts: (1) a substrate facies, (2) a lower mound facies, and (3) an upper mound facies. He also pointed out that *Komia* was an important component in the formation of algal mounds. He specifically described the upper mound facies as composed of *Komia* wackestone and packstone deposited in near-wave-base environments that formed extensive flanking beds.

Weber (1995) conducted further examination of the Caddo algal mounds in Stephens County. On the basis of stratigraphic position within the Caddo, he described a three-fold division at the Caddo Limestone: (1) biogenic bank, (2) grainstone/packstone shoal, and (3) an algal-mound complex. Between the biogenic bank and the algal-mound complex located in the grainstone/packstone shoal is a sequence of bioclasts up to 40 ft thick (Weber, 1995). Weber (1995) interpreted the uppermost unit of the Caddo Limestone as an algal-mound complex, made of phylloid algal and *Komia* remains, and carbonate mud.

Based on cores, Miller (2001) interpreted six depositional lithofacies and used petrophysical logs to correlate the cored wells with other wells to propose a regional depositional history. He also determined an approximate age of the Caddo algal mound intervals from the paragenetic sequence (Miller, 2001).

Loucks and Fu (2016) conducted research characterizing the lithofacies and dual micropore/macropore network in the shelf-buildup complexes of the Caddo Limestone. Seven lithofacies types were more specifically defined using criteria Dunham's (1962) carbonate classification. These facies fit into a coherent depositional model that could be tied into higher orders of relative sea-level changes (Loucks and Fu, 2016). Their research brought attention to the relation between reservoir quality, facies types, and depositional environments. The diagenesis study provided an insight to the formation of porosity within the Caddo Limestone. By analyzing porosity and permeability based on thin sections, core plugs and wireline logs, the article cited some possible lithofacies as being good hydrocarbon reservoir rocks.

Fu et al. (2017) focused on the main reservoirs formed in the upper and middle intervals of the Caddo algal mounds because of meteoric dissolution. Those authors quantified the average porosity value of *Komia* wackestone and packstone, phylloid-algal wackestone and packstone, and bioclast packstone with the core samples from seven wells. And based on the porosity and permeability analysis, the authors concluded that *Komia* wackestone and packstone are major reservoir rocks.

Previous studies of the carbonate mounds of the Caddo Limestone have progressed from qualitative to quantitative, with the help of advanced technologies and more accurate data. As can be read from the previous articles (Weber, 1995; Miller, 2001; Loucks and Fu, 2016), deeper understanding of *Komia* and phylloid algae has been obtained, more detailed lithofacies have been classified, and depositional environments have been defined. Driven by the production activity at the Fort Worth Basin, porosity types have been tied to lithofacies to help determine good-quality reservoirs. However, no studies have focused on constructing a lithofacies map of the Caddo Limestone. Because the carbonate mounds in Stephens County should be further investigated in

terms of their internal architecture, which will be significant for reservoir characterization in future studies, this research project focuses in detail on the lithofacies distributions by constructing a three-dimensional lithofacies map using *petrel* of the Eliasville Oil Field in Stephens County.

Research Objectives

Compared to pure siliclastic reservoirs, carbonate reservoirs invariably display much more heterogeneity, thus making their characterization more complicated (Colacicchi and Baldanza, 1986). Previous work on the characterization of the Caddo Limestone reservoirs have focused on the qualitative description of facies and their pore network and petrophysical properties.

This study constructs a detailed three dimensional geocellular model of the lithofacies distribution of the Caddo Limestone in Eliasville Field.

Specific outcomes include

1. Identifying the lithofacies from cores and thin sections.
2. Interpreting seismic data to construct a detailed structural map of Cycle A and Cycle B in the upper Caddo Limestone.
3. Interpreting well log data and conducting correlations and calibrations with cores.
4. Applying an artificial neural network to conduct facies simulation and predict lithofacies distribution in each well without cores, and extrapolating predictions of lithofacies in areas between wells.
5. Providing a detailed map of lithofacies distribution based on well logs, cores, statistical analysis, and neural network simulation.

Geological Setting

Regional Setting

The Pennsylvanian (early Desmoinesian) Caddo Limestone is located in North-Central Texas. Maximum thickness of the Caddo Limestone is 800 ft (Forehand, 1991). The carbonate mound complexes were distributed at the uppermost section and the deposition took place during early Desmoinesian (Turner, 1957). These mounds were deposited on the eastern side of the Concho Carbonate Platform (Figure 2-1).

Formation of these mounds was facilitated by the regional tectonic setting, controlled by the Fort Worth Basin, the Concho Platform, the Bend Arch, and the Ouachita Thrust Belt (Miller, 2001). The Ouachita thrust belt, a 2000-km-long band of deformed Paleozoic rocks, marks the southern margin of the North American craton (Grayson et al., 1987). The Fort Worth Basin came into being through initial downwarping between the Concho Platform and the Ouachita thrust belt, during the continental collision of Gondwana and Laurasia (Jarvie et al., 2007). This collision induced tectonic loading of the western Ouachita thrust belt, thus forming a large triangular-shaped foreland basin, the Fort Worth Basin (Grayson et al., 1987, Figure 2-1).

On the Concho Platform are two important arches, the Bend Arch and the Concho Arch. The Bend Arch marks the eastern border of the Concho Platform and the western flank of the Fort Worth Basin (Melnyk and Maddocks, 1988). This north-south-trending positive relief structure formed in Pennsylvanian time as a flexural hinge of the Fort Worth Basin (Cleaves, 2000). The flexural hinge was down warped and migrated westward when the sediments from the Ouachita thrust belt filled the basin (Dihlberg, 1989). The Concho Arch approximately aligned in the same northwest-southeast direction as algal mounds at the Concho Carbonate Platform.

The Pennsylvanian (early Desmoinesian) Caddo Limestone, having abundant *Komia* and phylloid algal mound complexes in its uppermost section, was deposited along the eastern flank of the Concho Platform (Johnson, 1988). Two siliciclastic depositional systems, the Atoka delta and the Strawn fluvial system, dominated the filling of the Fort Worth Basin and significantly affected carbonate production in the Concho Platform (Miller, 2001). During Atokan time, the Atokan delta gradually filled the Fort Worth Basin with sediments from the Ouachita thrust belt. In the middle of Atokan, the subsidence of tectonics was rather active and trapped all the clastic sediments at the Fort Worth Basin (Kier, 1980). The deposition of platform carbonates took place in the entire Concho Platform, but large carbonate algal banks formed mainly in the eastern margin of the platform (Cleaves, 2000), which is the focus of this research.

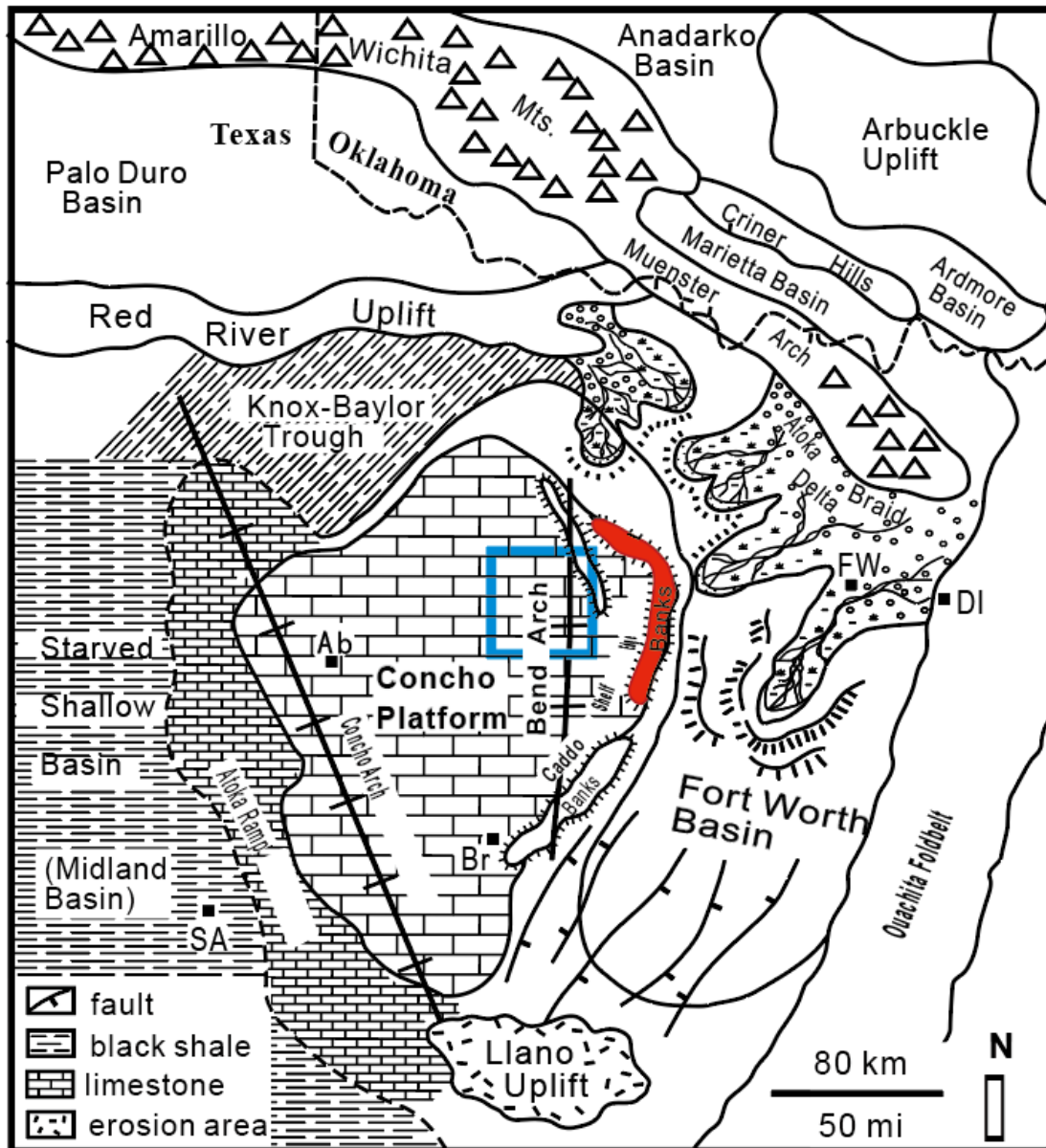


Figure 2: Paleogeographic map of Desmoinesian structures, showing structural elements and depositional systems in North-Central and West-Central Texas. Rectangle in the center of the diagram indicates location of Stephens County. Cities: Ab = Abilene; Br = Brownwood; DL = Dallas; FW = Fort Worth; SA = San Angelo. The red area indicates the boundary between the Concho Platform and the Fort Worth Basin. Modified after Fu et al. (2017), based on Yancey and Cleaves (1990), and Cleaves (2000).

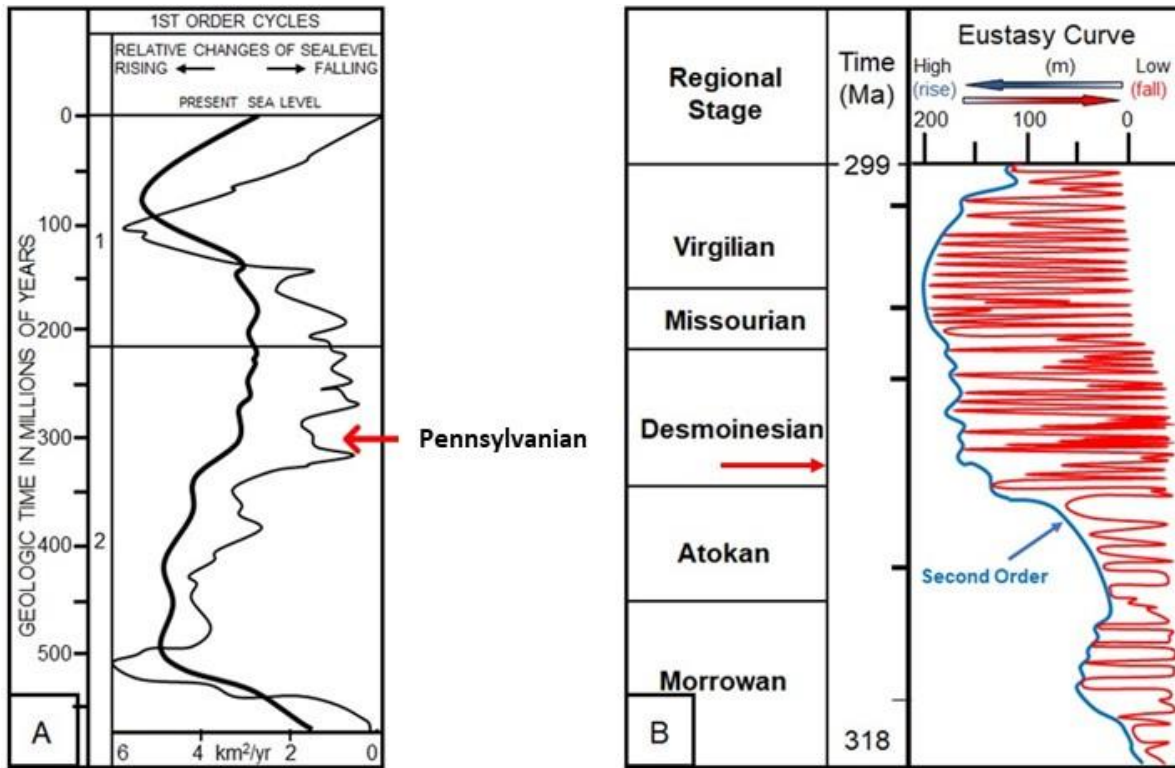


Figure 3: (A) Geologic timeline showing the 1st-order curve with respect to present-day sea level, the rate of production of ocean crust, and the condition of glaciation. After *Plint et al. (1992)*. (B) Plot of relative change in eustasy in the late Pennsylvanian. Blue curve shows the 2nd-order cycles and the red curve showing the 3rd-order cycles. Red arrow indicated the sea-level variation in the early Desmoinesian. Modified after *Ross and Ross (1987)* and *Wright (2011)*.

Besides the tectonic activity, relative sea-level variation is also an important contributor to the carbonate deposition in the Caddo Limestone. Pennsylvanian (early Desmoinesian) cycles were strongly influenced by glaciation, which produced high frequencies of relative sea-level changes (Figure 2.2) (*Cleaves, 2000*). Under icehouse conditions, carbonate depositions formed well-defined cycles and widespread meteoric diagenesis (*Follmi, 1995*). In this study area, three cycles of phylloid algal mound deposition were described by several authors (e.g., *Miller, 2001*). Diagenesis is also very common, and a well-developed pore system has been studied by a few investigators, e.g., *Qilong Fu and Bob Loucks*.

Local Stratigraphy

The Pennsylvanian stratigraphy of the Stephens County in North-Central Texas displays a repetitive occurrence of carbonate and siliciclastic deposition (Pollastro, 2007).

There are three sequences in the Pennsylvanian: from the oldest to the youngest, (1) the Lower and the Upper Marble Falls Limestone, (2) the Smithwick Shale, and (3) the Caddo Limestone.

The Caddo Limestone is at the top of the Smithwick Shale, spanning the Late Atokan Stage to the Early Desmoinesian Stage (Van Waggoner, 1977). The Caddo Limestone is an approximately 800-ft thick continuous succession (Turner, 1957). The lower intervals of the Caddo are Atokan in age, whereas the upper part is Desmoinesian in age (Turner, 1957). The study intervals, Cycle A and Cycle B, are located at the top of the Caddo Limestone, containing Desmoinesian algal mounds.

On top of the Caddo Limestone are the prodeltaic and basinal shales of the Strawn Group (Grayson et al., 1987). The interval above Cycle A and Cycle B is also reported to be a second interval of the Smithwick Shale, because of the lithologic similarity of the Desmoinesian Strawn prodeltaic and basinal facies to the Atokan Smithwick Shale (Day-Stirrat and Van Waggoner, 2008).

Local stratigraphy at the North-Central Texas resulted from the interaction of the Ouachita thrust belt, the Fort Worth Basin, and migration of the Bend Flexural Arch and the Concho Platform where the carbonate sediments were deposited (Saller et al., 1999).

System	Stage	Group and Formation			
Carboniferous	Pennsylvanian	Virgilian	Cisco Group		
		Missourian	Canyon Group		
		Desmoinesian	Strawn Group	(upper Smithwick Shale at the base)	
				Caddo Limestone	
		Atokan	Bend Group	(lower Smithwick Shale)	
	Morrowan	Upper Marble Falls Limestone (Big Saline Formation)			
		Lower Marble Falls Limestone (Comyn Formation)			
	Mississippian	Chesterian	Barnett Shale		
		Meramecian			
		Osagean	Chappel Limestone		

Figure 4: Stratigraphic chart of Mississippian and Pennsylvanian in Stephens County, North-Central Texas. After Fu et al., 2017, modified from Cheney and Gross, 1952; Brown, 1973; Weber, 1995; Pollastro et al., 2007.

Methodologies and Dataset

Throughout this research project, core descriptions were coupled with thin-section observations. To better view and describe the texture and allochems of the rocks, the cores were slabbed on May 20th 2017, and dilute HCl acid was applied to the 2/3 sample halves to clean the surface. Lithofacies were described using Dunham's (1962) classification criteria. Thin sections were made to help classify the facies.

After defining the lithofacies qualitatively, both geological descriptions and well-log data were input into a geomodelling software to build a 3D reservoir model. Based on the gamma-ray curve of wireline-log data, the tops of Cycle A and Cycle B were picked so as to construct the structural maps, from which the mounds can be shown. To improve the accuracy of the map, the interpreted seismic data were input into *Petrel* to make the formation structure more detailed and reliable. After the structural maps of Cycle A and Cycle B were established, the lithofacies were defined on the map based on the core description coupled with well log data. An artificial Neural Network (ANN) was an important tool used in predicting the lithofacies distribution on the wells for those without core data. The study applied machine learning to two wells with both complete well log data and core data. The ANN conducted mutual-learning to generate a set of algorithms to make predictions about the lithofacies. Relevant parameters were adjusted to acquire the best fit sets of algorithms for the whole field (Jung and Aigner, 2012).

After the predicted lithofacies were generated for each well, a regular 3D grid was constructed using 125 stratigraphic surfaces built from well logs and 3D seismic data. The lithofacies interpreted at each well were extrapolated throughout the grid using an indicator Kriging algorithm (Moinard, 1987).

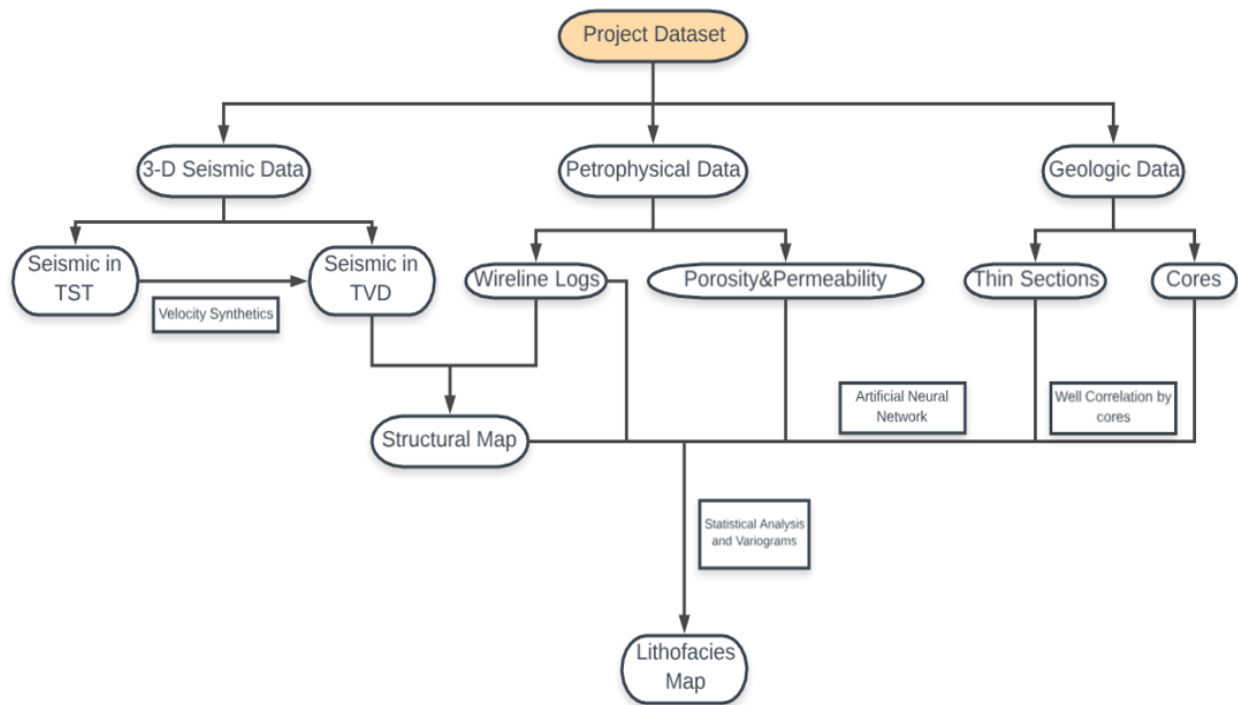


Figure 5: Flow chart of the study involving 3-D seismic data, geologic data, and petrophysical data

The data comprise three-dimensional seismic data, wireline logs, and geologic data (Figure 3-1). Based on the 3-D seismic data and well logs, a structural map can be constructed. Cores and thin sections were coupled with wireline logs to make the lithofacies distribution map.

Petrographic Observation

Core study

There are 18 cores from Eliasville and East Eliasville Fields. Approximately 700 ft (220 meters) of slabbed cores from 12 wells were described. Samples were taken at the Bureau of Economic Geology (BEG) Core Research Center (CRC) in Austin, Texas.

Table 1: Cored wells in Stephens County, North-Central Texas

API Number	Well Name	Operator	Field	Core Length (feet)	Surface X	Surface Y
42429321020000	Atkins, A.A. #13	Texas Pacific Oil Co	East Eliasville	62	31.6666667	97.5000000
42429310970000	Kirkland, I.E. #A-6	Texas Pacific Oil Co	East Eliasville	26	31.6666667	97.5000000
42429310190000	Newell, Dell #1	Texas Pacific Oil Co	East Eliasville	49	31.6666667	97.5000000
42429310740000	Newell, Dell #2	Texas Pacific Oil Co	East Eliasville	71	31.6666667	97.5000000
42429310340000	Eliasville Caddo #33	Texas Pacific Oil Co	Eliasville	60	31.6666667	97.5000000
42429312280000	Eliasville Caddo #79	Texas Pacific Oil Co	Eliasville	72	31.6666667	97.5000000
42429309810000	Hill, G.W. Acct. 2 #5	Texas Pacific Oil Co	Eliasville	52	31.6666667	97.5000000
42429312610000	Eliasville Caddo #106	Basa	Eliasville	62	31.6666667	97.5000000
42429334450000	Eliasville Caddo #131	Basa	Eliasville	59	31.6666667	97.5000000
42429311660000	Eliasville Caddo #46	Basa	Eliasville	56	31.6666667	97.5000000
42429313030000	Eliasville Caddo #86	Basa	Eliasville	51	31.6666667	97.5000000
42429305290000	Atkins, A.A. #5	Clark Lester	East Eliasville	52	31.6666667	97.5000000

Thin sections

In this study 18 thin sections were acquired from 4 different cores to better characterize the allochems, porosity, and lithofacies. These samples were prepared at TPS Enterprises LLC, Houston, TX. Half of the thin sections for carbonate rocks were stained with a mixed Alizarin red S/potassium ferricyanide solution to differentiate dolomite from calcite and were examined using a Zeiss Axioskop 40 microscope at the EPS Microscope Lab, at the Jackson School of Geosciences. Results of thin section analysis were in the form of microscope images taken by a SONY NEX-VG10 camera.

Wireline logs

The study area has 173 wells with wireline logs. Well data include gamma-ray curves (GR), spontaneous potential curves (SP), density curves (RHOB), density porosity (PHI), effective porosity curves (PHIE), total porosity curves (PHIT), neutron porosity curves (NPHI), sonic logs (DT), medium induction resistivity logs (ILM), and deep induction resistivity logs (ILD). GR was utilized to define Cycle A and Cycle B. Spontaneous potential data were used to convert the 3-D seismic data from the time zone to the depth zone. Six logs — GR, RHOB, PHIE, PHIT, ILM and ILD — were applied to the artificial neural network for simulation purposes.

Three-Dimensional seismic data

An understanding of the three-dimensional distribution of lithofacies resulted from integration of all available data into a 3-D stratigraphic model (Tinker et al., 2004). The 3-D seismic data from Eliasville Field consist of a 53 x 55 mile survey. Synthetic seismograms were generated using velocity data from the sonic log and density data from the density log. The synthetic seismic trace closely approximated a trace from a seismic line that passed close to the

well in which the logs were acquired (Kenter et al., 2002). The synthetic was then correlated with both the seismic data and the well log from which it was generated.

Lithofacies

Structure Map

Structure maps were constructed based on well correlation using the well log data of GR and RHOB. Cross section **I** is the strike-direction correlation, and Cross section **II** is the dip-direction correlation. The boundary between the upper shale and the Caddo Limestone is denoted by the GR value of approximately 75. Cycle A and Cycle B values were obtained based on gamma-ray data with the help of density log (RHOB). Due to the depths limitations of the well logs and cores, this research focuses on the modelling of Cycle A and Cycle B only. Almost all wells in the study area terminated in Cycle A or Cycle B.

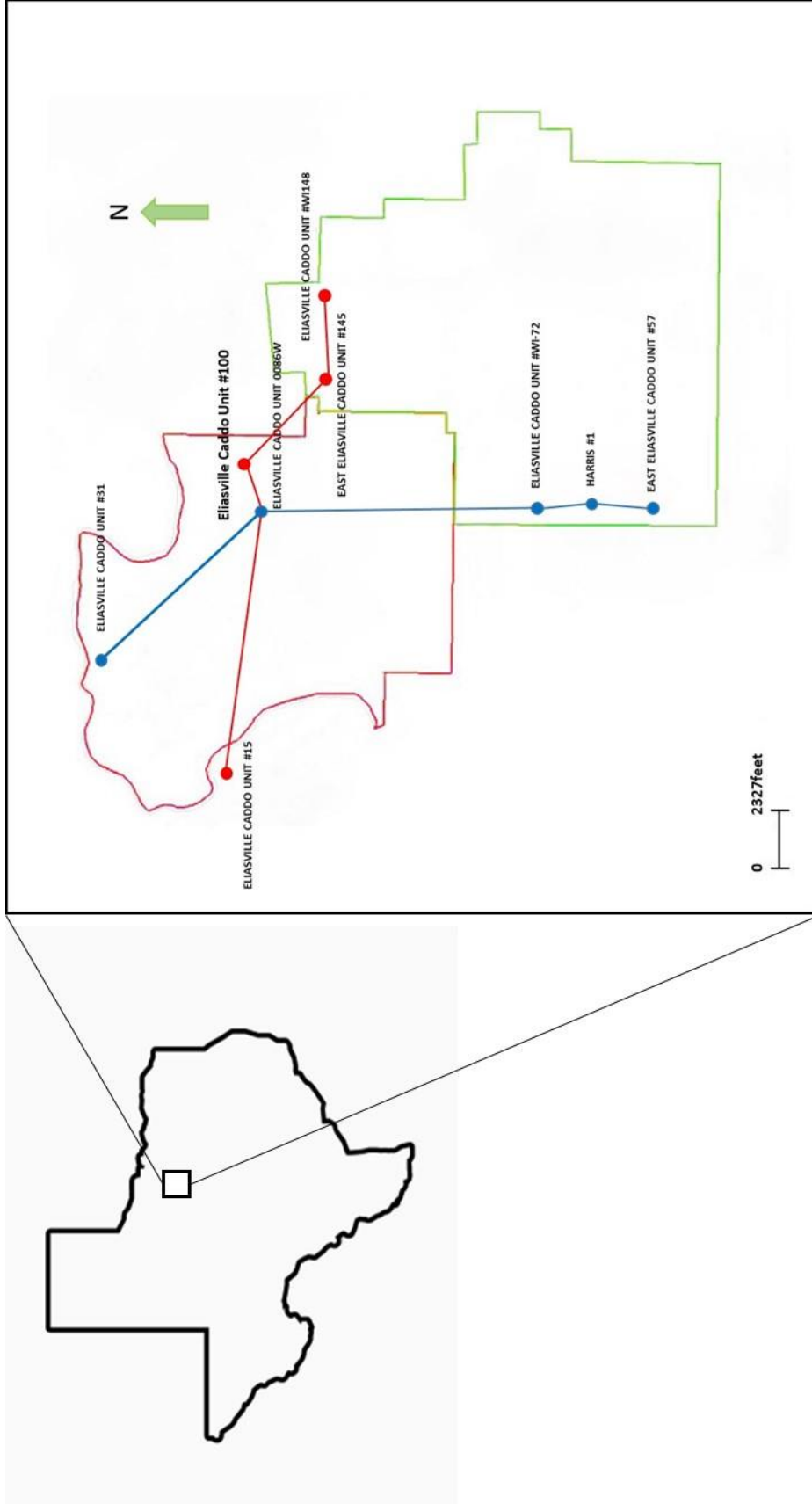


Figure 6: Map of Eliasville and East Eliasville Fields. The red boundary shows the field of Eliasville and the green boundary shows the East Eliasville Field. The red line and the blue line represent cross sections **I** and **II**, respectively.

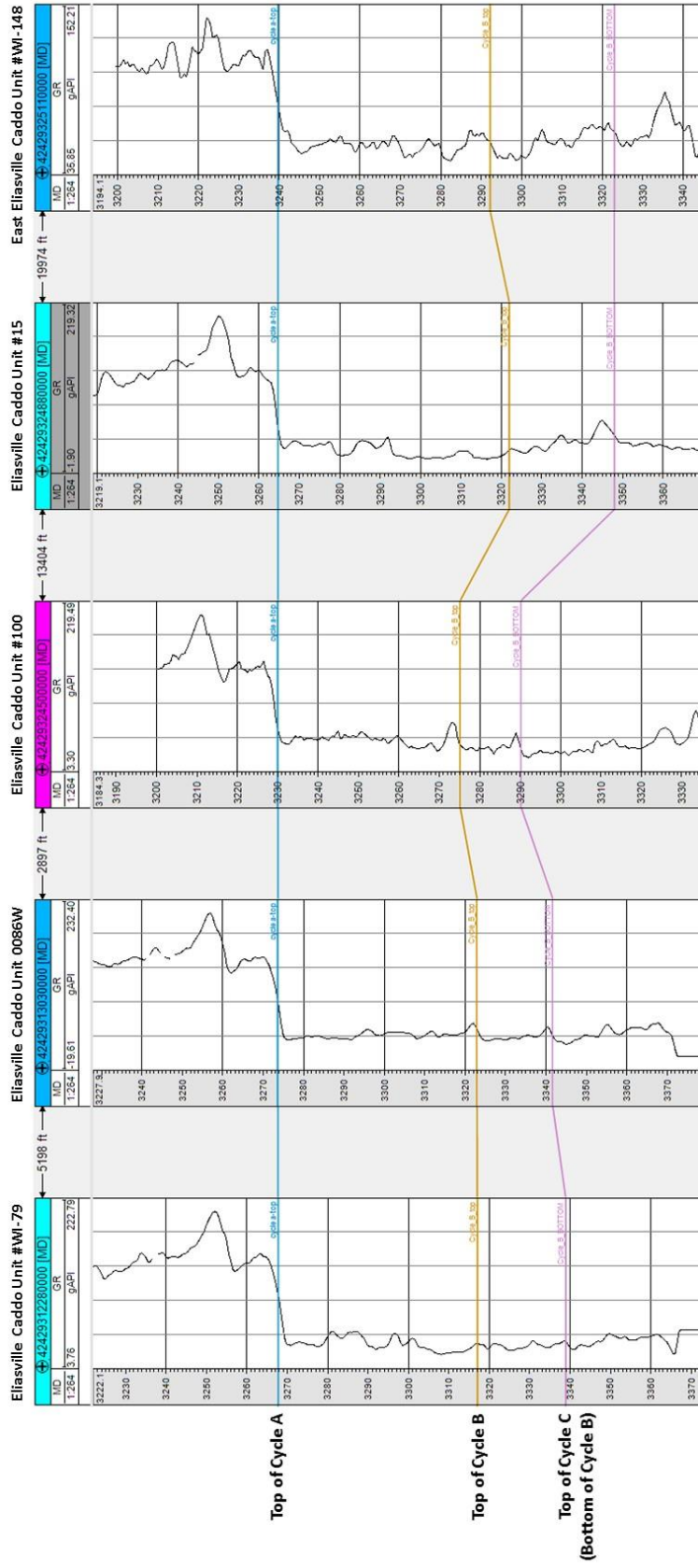


Figure 7: Stratigraphic cross section I showing Cycle A and Cycle B in the Caddo Limestone, based on wireline logs (GR). See Figure 4-1 for the location of the cross section.

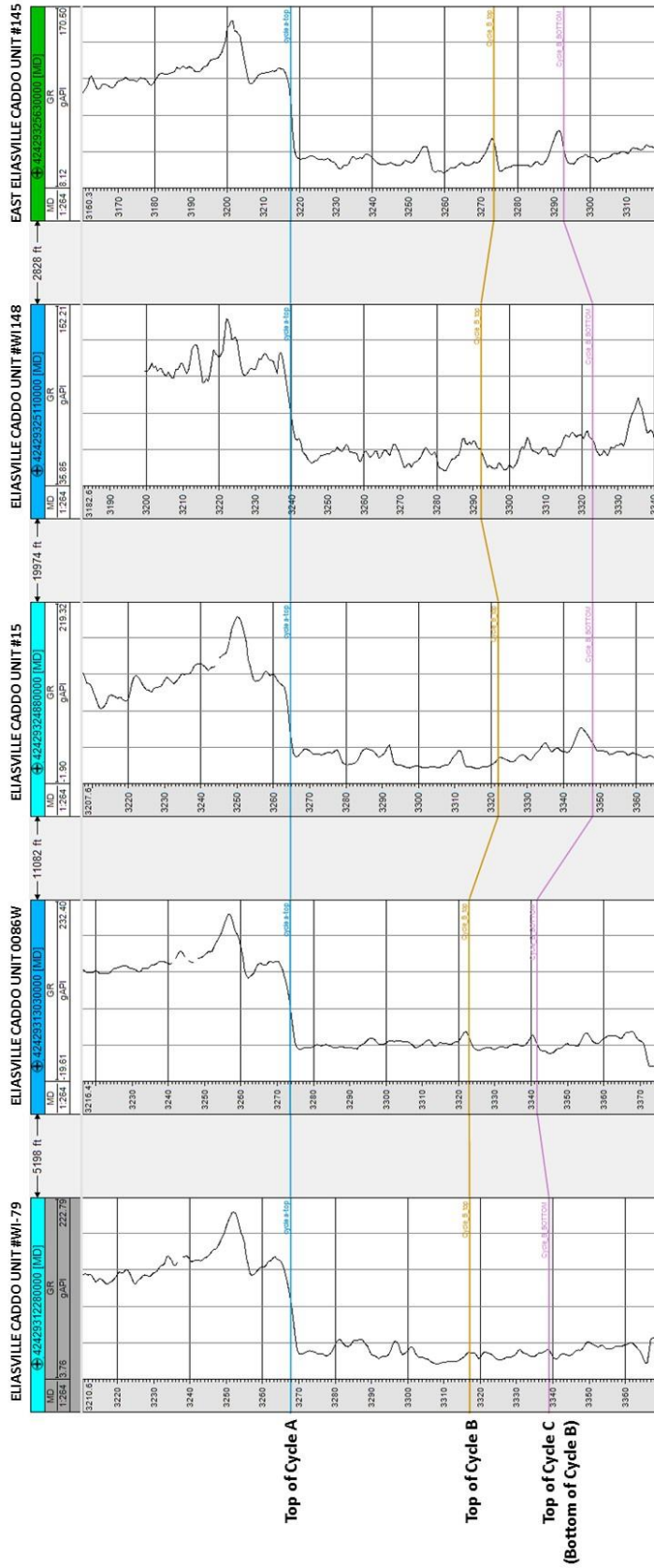


Figure 8: Stratigraphic cross section showing Cycle A and Cycle B in the Caddo Limestone, based on wireline logs (GR). See Figure 4-1 for the location of the cross section.

The structure map on the top of the Caddo Limestone was constructed using the 3-D seismic data and wireline-log data. Two carbonate mounds appear in the map. Their trend direction is approximately northwest to southeast. The northeast and the southwest edges of the map have no valid data, therefore, in these two edges the models are not reliable, which is denoted by L1 and L2.

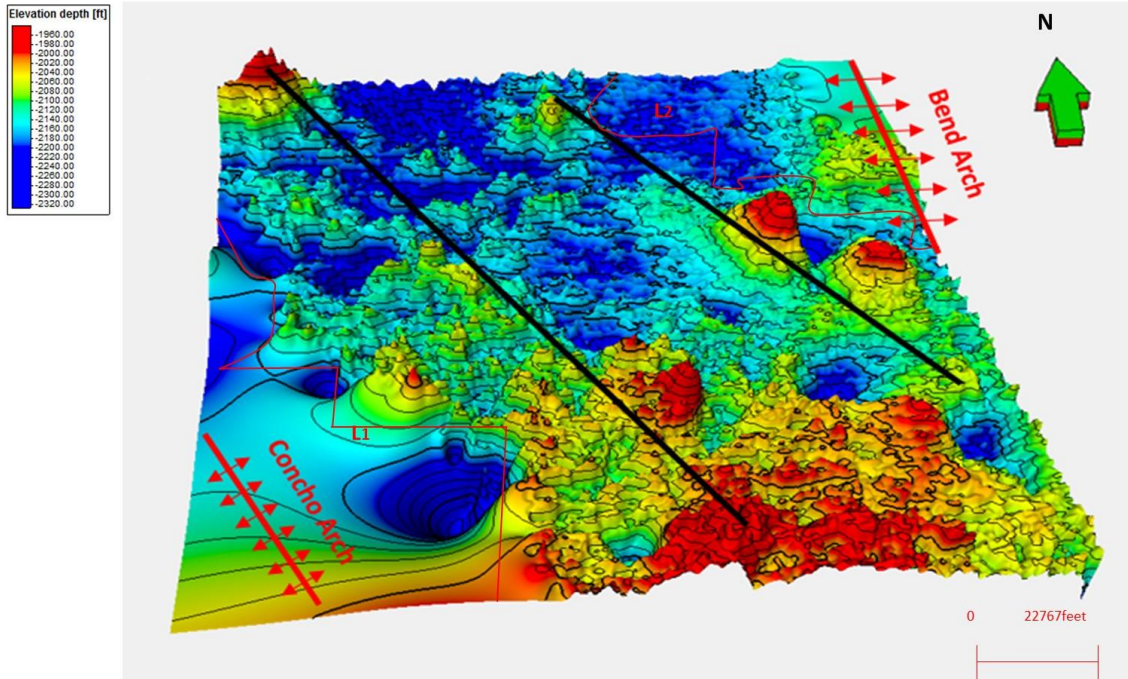
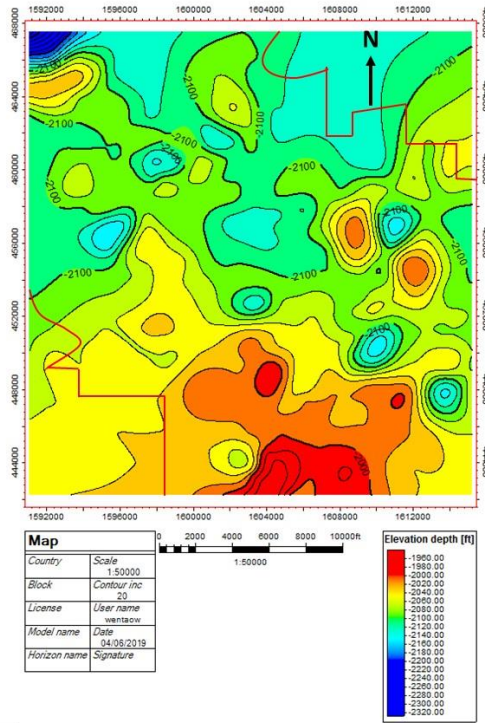
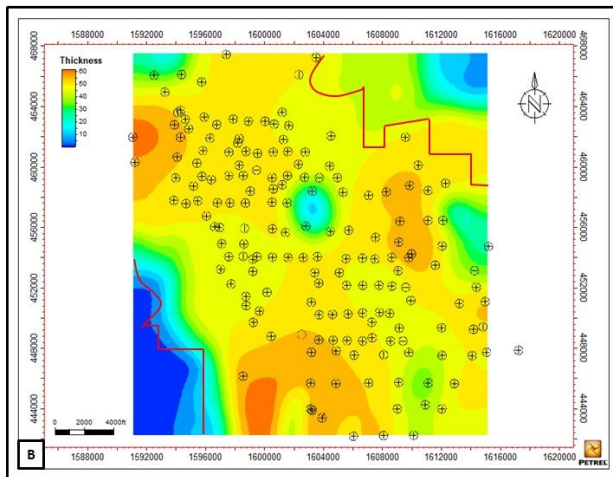


Figure 9: A 3D structure map on the top of the Caddo Limestone constructed from seismic data in the study area in which the alignments of carbonate mounds and the topographic highs are shown. The Northeast and Southwest edges of the map have no valid data, as denoted by two red boundaries, L1 and L2.

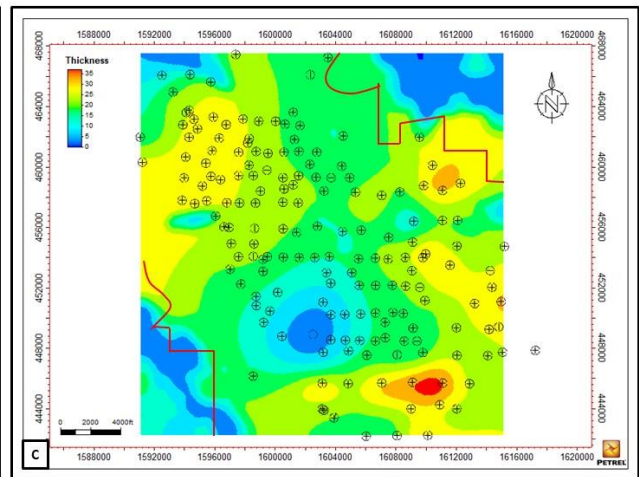
Mounds refer to locations of topographically higher elevation on any surface. Those two mounds in the structural map appear to be roughly parallel to the Concho Arch.



A



B



C

Figure 10: (A) A 2-D structure map interpreted from seismic data and wireline log data in the study area. The northeast and southwest edges of the map have no valid data, as denoted by two red boundaries. (B) Isochore map of the Cycle A interval in the Caddo Limestone showing variations in thickness from about 10 to 65 ft, established based on 173 wells shown on the map. (C) Isochore map of the Cycle B interval in the Caddo Limestone showing variations in thickness from approximately 0 to 40 ft, based on the 173 wells used on the map.

Lithofacies Descriptions

In this study, stratigraphic intervals present in the cores are in Cycle A and Cycle B. According to core descriptions and microscopic observations, five lithofacies were defined based on Dunham's (1962) carbonate classification slightly modified by Lucia (2007). There are three *Komia* lithofacies, one phylloid-algal lithofacies as well as one bioclast lithofacies. The lithofacies are: (1) *Komia* wackestone and mud-dominated packstone, (2) *Komia* grain-dominated packstone and grainstone, (3) *Komia* boundstone, (4) phylloid-algal wackestone, and packstone and (5) bioclast wackestone. Three major depositional environments have been determined for the Caddo Limestone, and each is represented by one or more types of lithofacies.

***Komia* wackestone and mud-dominated packstone**

Komia wackestone and mud-dominated packstone are the most common lithofacies in the cores and thin sections studied. They are light gray in color. *Komia* fragments are the dominant skeletal grains in the study area.

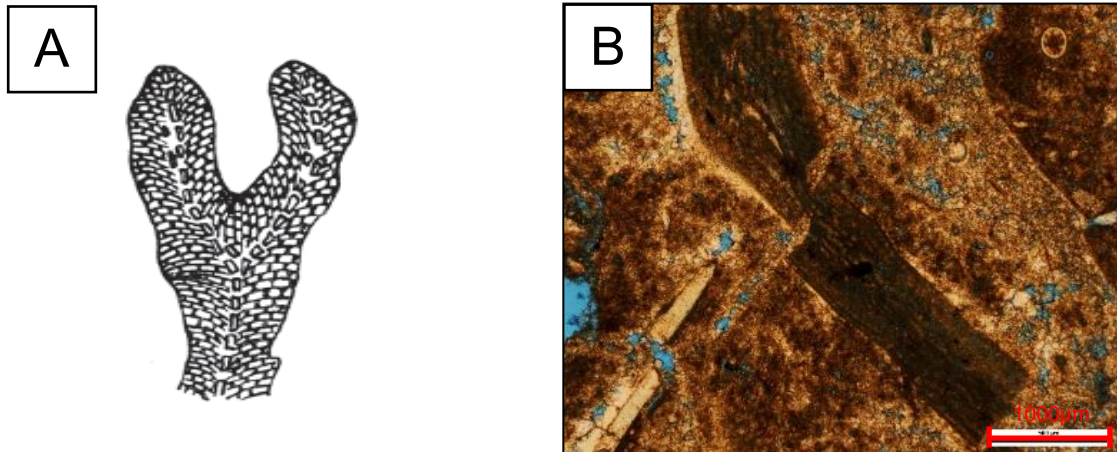


Figure 11: Diagrams of *Komia* (A) Schematic of *Komia* showing its internal structure (from Flügel, 2010). (B) Photomicrographs of *Komia* from the East Eliasville Caddo Unit #WI-115 well, 3367.9 ft.

Komia is abundant in *Komia* wackestone and mud-dominated packstone. Numerous minor allochems, such as echinoderms, bryozoans, foraminifers, brachiopods, ostracods, mollusks, and phylloid algae also appear in this lithofacies.

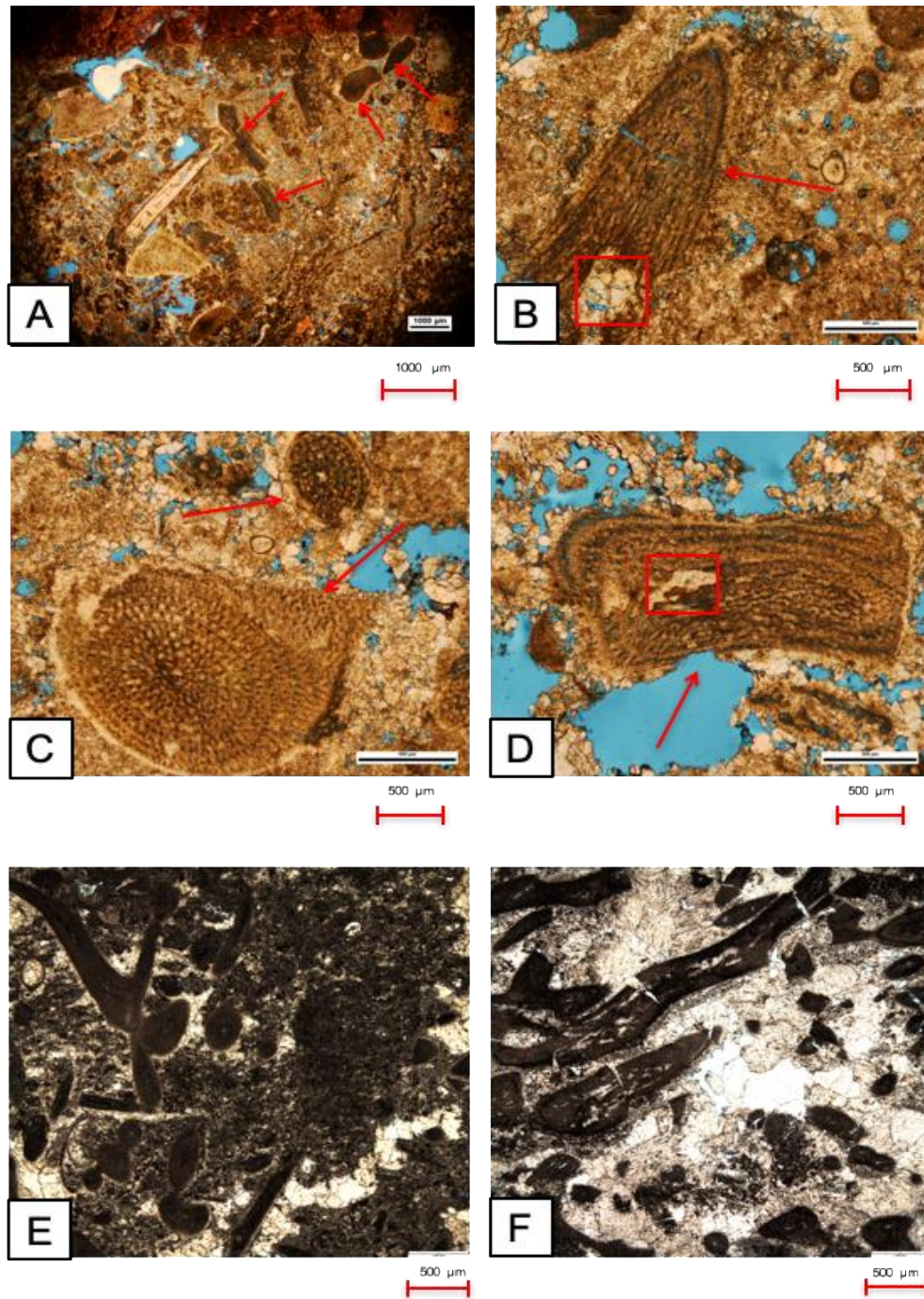


Figure 12: Photomicrographs of *Komia* lithofacies. (A) *Komia* wackestone; *Komia* is indicated by the red arrows. (B) *Komia* and calcite cement infilling an intragranular pore that resulted from dissolution, as is enclosed by the rectangle. (C) Stalk of *Komia* in the longitudinal section. (D) *Komia* fragments that diagenetically altered. (E) Lithofacies of *Komia* wackestone, courtesy of Qilong Fu. (F) *Komia* packstone with cemented intergranular pores.

Komia is predominant at the Caddo Limestone. The pore system is well-developed in the *Komia* lithofacies as this allochem is commonly associated with micropores and macropores. In Figure 4-7, intergranular and intragranular pores are abundant, although vuggy pores are the most common. This kind of large pore is a major contributor to hydrocarbon storage and flow. Thus, knowing the distribution of *Komia* lithofacies is significant for propagating reservoirs.

Bryozoans widely spread in *Komia* wackestone and mud-dominated packstone. Intragranular pores are also very common with bryozoans' fragments, with their diameters usually ranging from 75 μ m to 250 μ m.

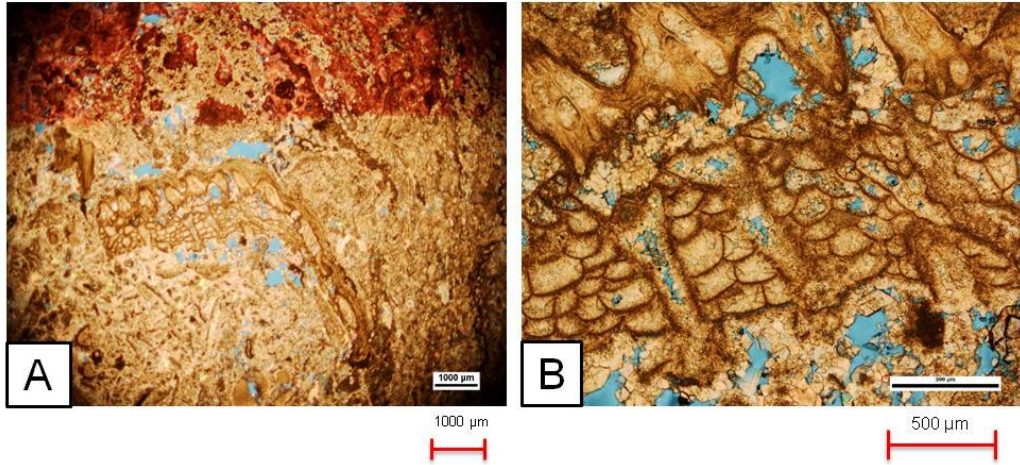


Figure 13: (A) Photomicrograph showing bryozoans, from the Newell Dell #2 well, 3383.81 ft. (B) An enlarged version of Figure (A) showing the detailed structure of bryozoans, micropores, and macropores.

Foraminifera are another widespread bioclast in *Komia* wackestone and packstone. Mililoid are common.

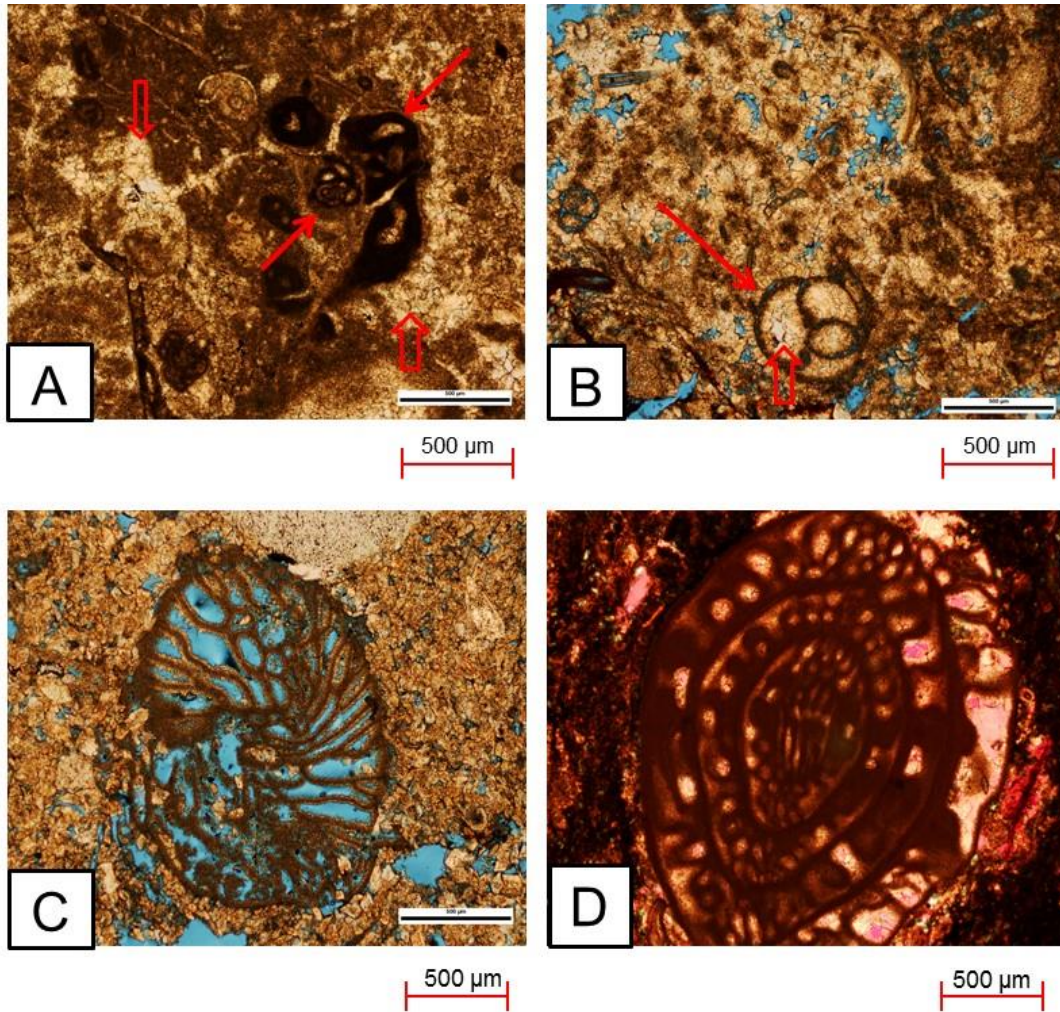


Figure 14: (A) Photomicrograph showing miliolid (solid red arrow) and cemented vugs (hollow arrow), from the Newell Dell #2 well, 3394.9 ft. (B) Photomicrograph demonstrating a completely cement-filled miliolid (solid red arrow), in which there are micropores (hollow arrow), from the NEWELL, DELL #2 well, 3367.9 ft. (C) Photomicrograph showing fusulinid with intragranular pores present and its matrix partially dissolved, through which more macropores were generated. (D) Photomicrograph demonstrating fusulinid – in which intragranular pores are completely occluded. Thin section was stained with Alizarin Red-S solution.

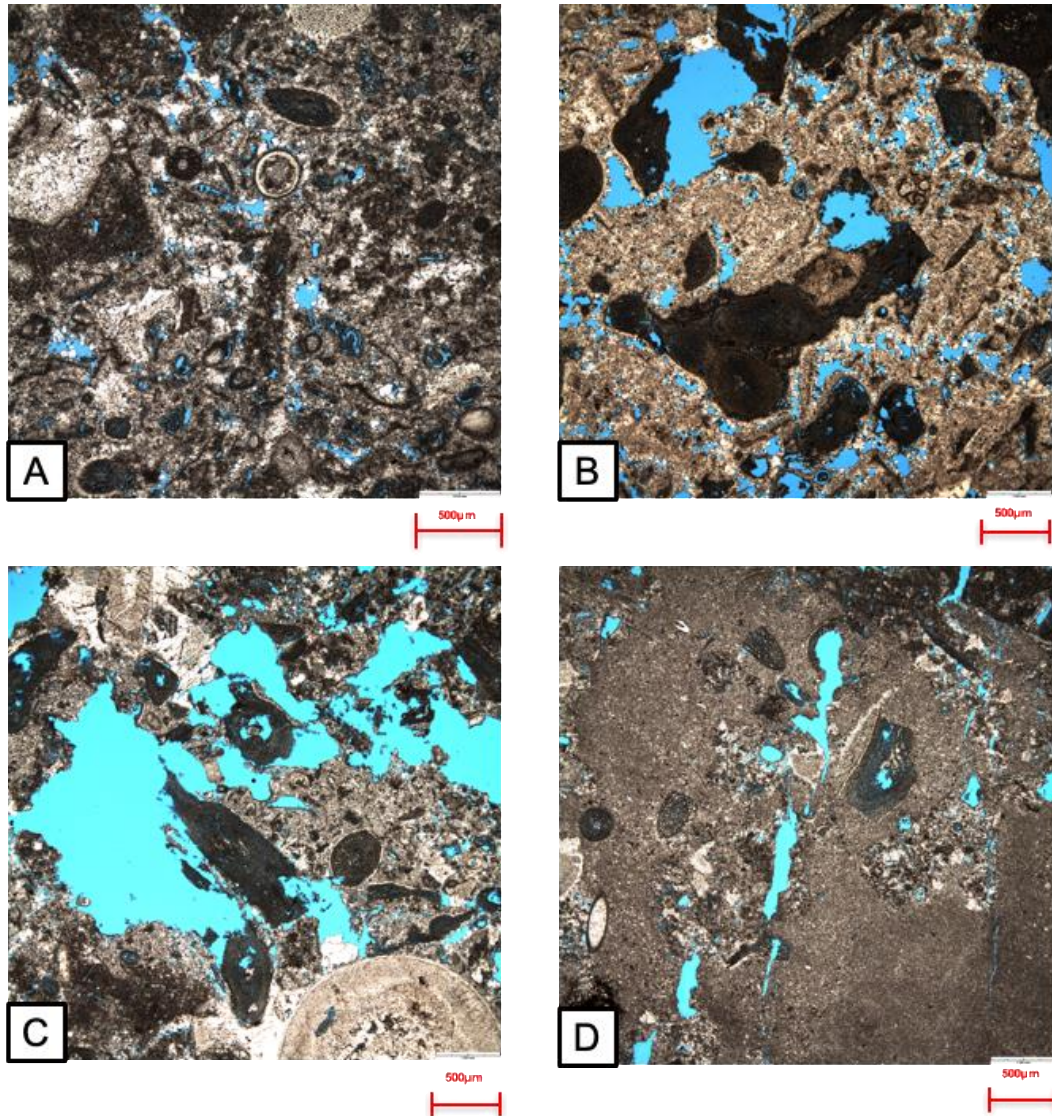


Figure 15: (A) Photomicrograph of *Komia* packstone with interparticle pores, from the Newell Dell #2 well, 3297.8 ft, courtesy of Qilong Fu. (B) Photomicrograph of *Komia* wackestone where most of the *Komia* are diagenetically altered, from the Newell Dell #2 well, 3289.5 ft. (C) Photomicrograph of *Komia* packstone with vuggy pores, from the Newell Dell #2 well, 3281.6 ft. (D) Photomicrograph of *Komia* wackestone showing cracks and channels, from the Newell Dell #2 well, 3274.0 ft, courtesy of Qilong Fu.

***Komia* grain-dominated packstone and grainstone**

Komia grain-dominated packstone and grainstone are light- to medium-gray limestone with abundant skeletal grains visible in the slabbed core. The bed thickness ranges from a few inches

to 8 ft. In some thin section samples, grains are composed almost entirely of *Komia* fragments. Fusulinids and echinoderms may be common skeletal grains in some samples. Other minor bioclasts are bryozoans, ostracods, gastropods and phylloid algae. Normal graded beddings are observed in slabbed cores.

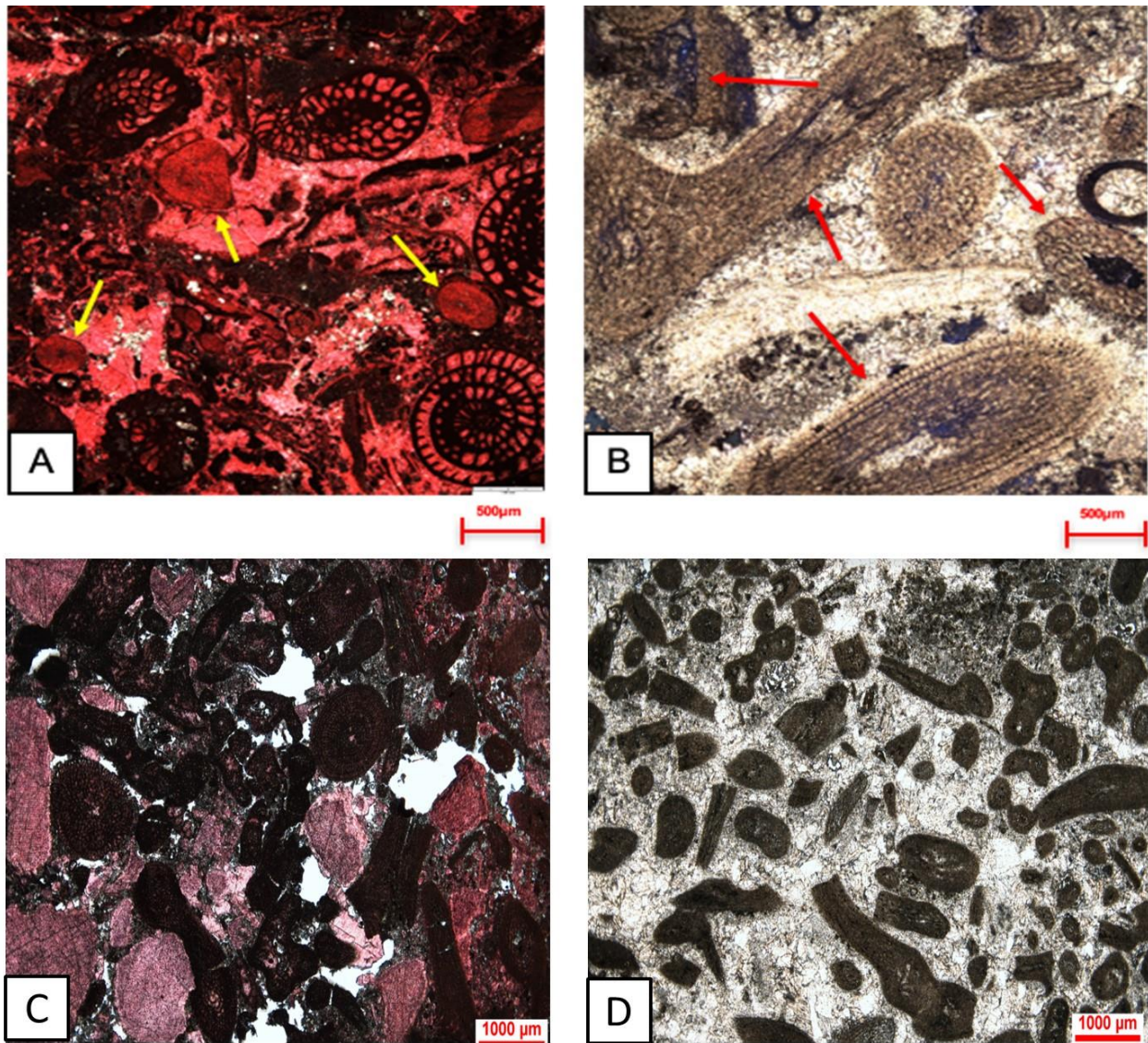


Figure 16: (A) Photomicrograph of *Komia* fusulinid grainstone where *Komia* is indicated by the yellow arrow. Calcite is stained with Alizarin Red-S solution. (B) Photomicrograph of *Komia* grain-dominated packstone with *Komia* indicated by the red arrow. (C) Photomicrograph of *Komia* grainstone. Calcite is stained with Alizarin Red-S solution, from the Newell Dell #2 well, 3222.2 ft. (D) Photomicrograph of *Komia* grain-dominated packstone, from the Eliasville Caddo Unit #106 well, 3261.6 ft.

Compared to *Komia* wackestone, *Komia* grain-dominated packstone and grainstone have much less or no lime mud matrix.

***Komia* boundstone**

Komia boundstones are the sedimentary rocks whose original components were bound together by the branches of *Komia* during deposition. This lithofacies is gray to yellowish gray. Maximum thickness of this lithofacies is 8 ft – however, most commonly the thickness of the bedding ranges from a few inches to 2 ft. The slender branches of *Komia* in this lithofacies are usually in a vertical growth position, which is clearly visible on the cores and thin sections. Comparatively, biotic diversity appears to be low in the *Komia* boundstones, and therefore other types of skeletal fragments are not commonly observed in this lithofacies.

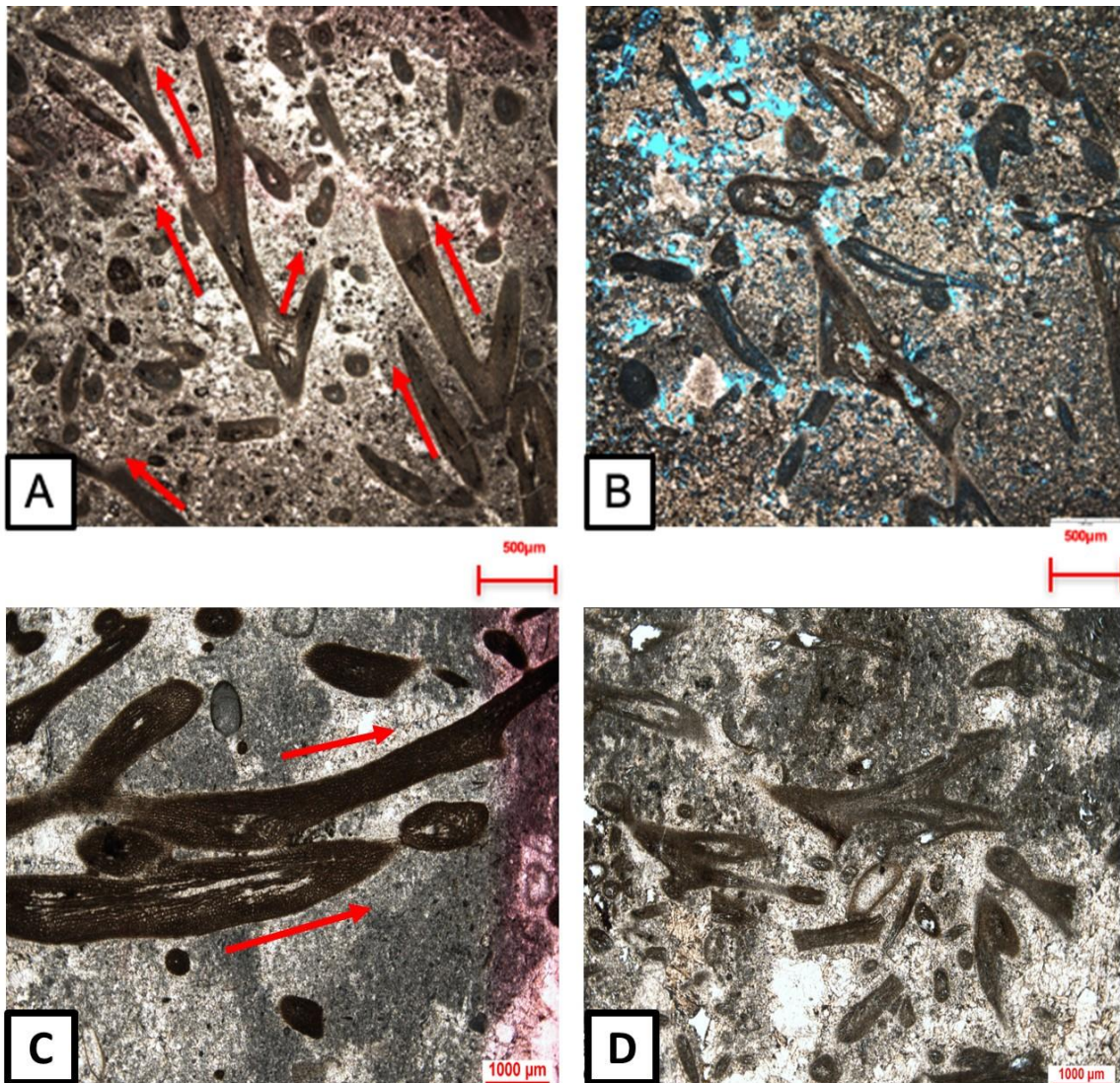


Figure 17: (A) Photomicrograph of *Komia* boundstone with red arrows indicating the growth direction of *Komia* thallus, from the Kirkland I.E. #A6 well, 3375.6 ft. (B) Photomicrograph of *Komia* boundstone showing intergranular and intragranular porosity, from the Newell Dell #2 well, 3270.3 ft. (C) Photomicrograph of *Komia* boundstone with red arrows indicating the growth direction of *Komia* thallus, from the Eliasville Caddo Unit #106 well, 3311.5 ft. (D) Photomicrograph of *Komia* boundstone showing relatively complete *Komia* thallus, from the Newell Dell #2 well, 3245.2 ft.

The thallus of *Komia* acts as an effective baffle to energy flows, like waves and currents, and it allowed fine-grain mud particles or peloids to be baffled and trapped. *Komia* in this lithofacies are usually more complete in shape than in other *Komia* lithofacies. *Komia* boundstone is less

porous than other *Komia* lithofacies. Additionally, *Komia* can endure higher energy than phylloid algae, which makes *Komia* boundstones able to grow in higher energy settings than phylloid-algal lithofacies. Abundant *Komia* can be clearly seen on slabbed core samples.

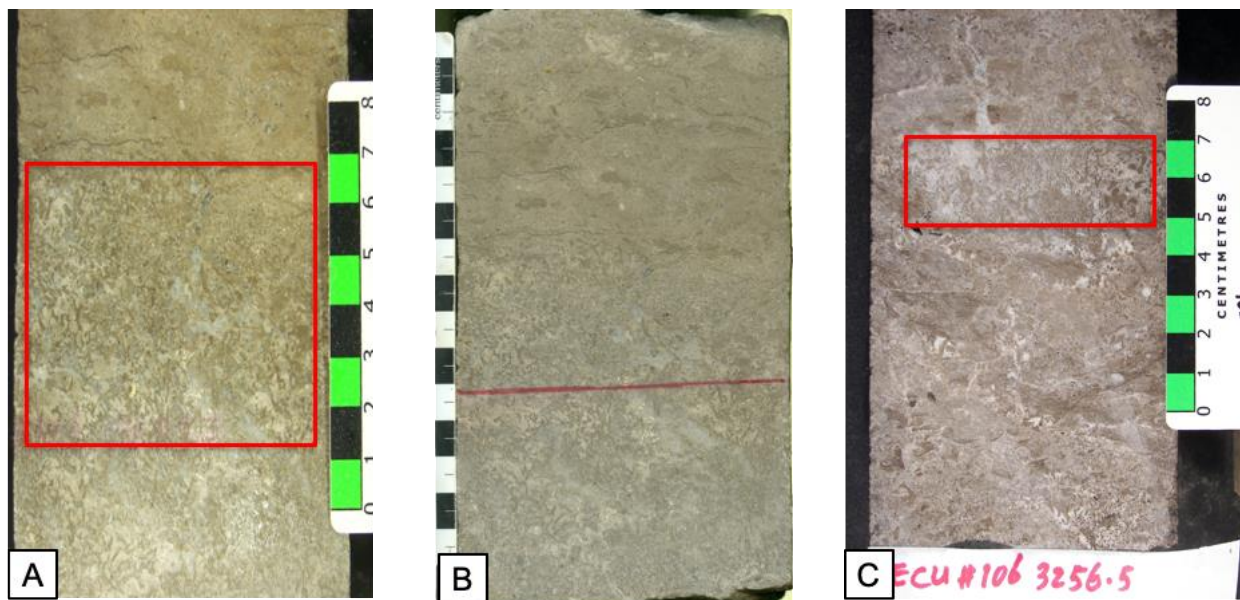


Figure 18: (A) Kirkland I.E. #A6 well, core sample of *Komia* boundstone, *Komia in situ* growth. (B) Eliasville #106 well, 3242.8 to 3243.4 ft. (C) Eliasville #106 well, 3256.5 ft, core sample of *Komia* boundstone, courtesy of Qilong Fu.

Phylloid-algal wackestone and packstone

Phylloid algal wackestone varies in color from light- to medium-gray to a yellowish-gray in slabbed cores. This type of lithofacies, with a thickness of 1 inch to 8 ft, mostly appear only in Cycle A at the Caddo Limestone. The most predominant allochems in this litho-type are phylloid algae – these rocks contain algal blades in different sizes with much trapped carbonate mud. Other minor bioclasts include brachiopods, echinoderms, foraminifers, brachiopods, ostracods, bryozoans, and some *Komia*.

In the thin sections, the phylloid algal blades appear to be long and thin, showing a sinuous form. Phylloid algal at Caddo Limestone have experienced extensive dissolution and

recrystallization across the entire phylloid-algal lithofacies. Large phylloid blades are either large moldic porosity or thin patches of mosaic calcite. Commonly, those phylloid algal blades are normally embedded in lime mud, which forms wackestones or mud-dominated packstones.

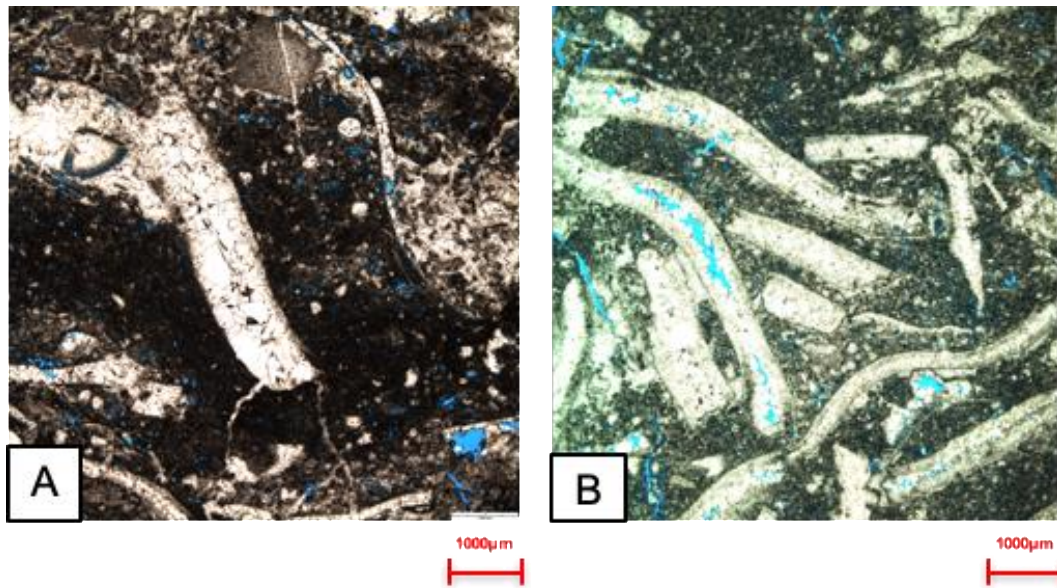


Figure 19: (A) Photomicrograph showing phylloid-algal wackestone, where the phylloid-algal blades have gone through extensive diagenesis, from the Newell Dell #2 well, 3217 ft. (B) Photomicrograph demonstrating phylloid-algal wackestone with a well-developed porosity system within the blades, where micro- and macro-pores were generated through diagenesis, from the Newell Dell #2 well, 3210 ft. Photomicrographs courtesy of Qilong Fu.

Phylloid algae can be clearly seen from the slabbed cores. Stylolites are commonly observed within phylloid-algal lithofacies. In Figure 4-14(A), horizontal stylolites are located below a mass of phylloid algae, shown in the rectangle.

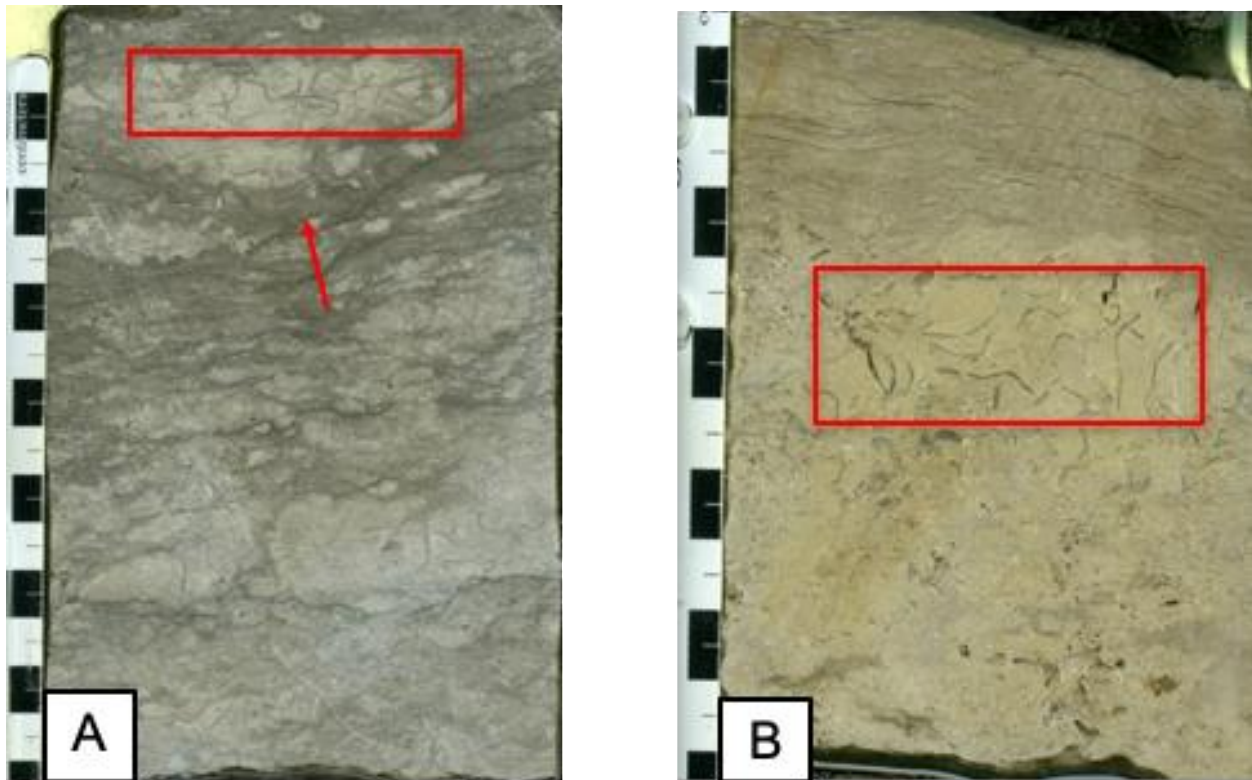


Figure 20: (A) Eliasville Caddo Unit #33 well, 3244.1-3244.6 ft, phylloid-algal wackestone with phylloid algae in the rectangle and stylolite indicated by the arrow. (B) Ward #97 well, 3170.2 - 3170.5 ft, phylloid-algal wackestone showing large, sinuous phylloid-algal blades on the surface. Photo courtesy of Qilong Fu.

In the Caddo Limestone, phylloid-algal wackestone and packstone constitute one of the major lithofacies in the Eliasville field. Large sinuous phylloid-algal blades are present, and vuggy pores can be clearly viewed. Phylloid-algal wackestone and packstone appear to be one of the most important lithofacies that bears hydrocarbon.

Bioclast wackestone to packstone

Bioclast wackestone to packstone is characterized in the core by light to dark gray beds. Thickness ranges from 2 inches to 11 ft. Compared to *Komia* and phylloid algae lithofacies, bioclast wackestone to packstones reveal a much more diverse faunal assemblage in which no

allochems are predominant. The composition of skeletal grains varies from sample to sample and includes fragments of *Komia*, phylloid algae, foraminifers, brachiopods, bryozoans, and crinoids.

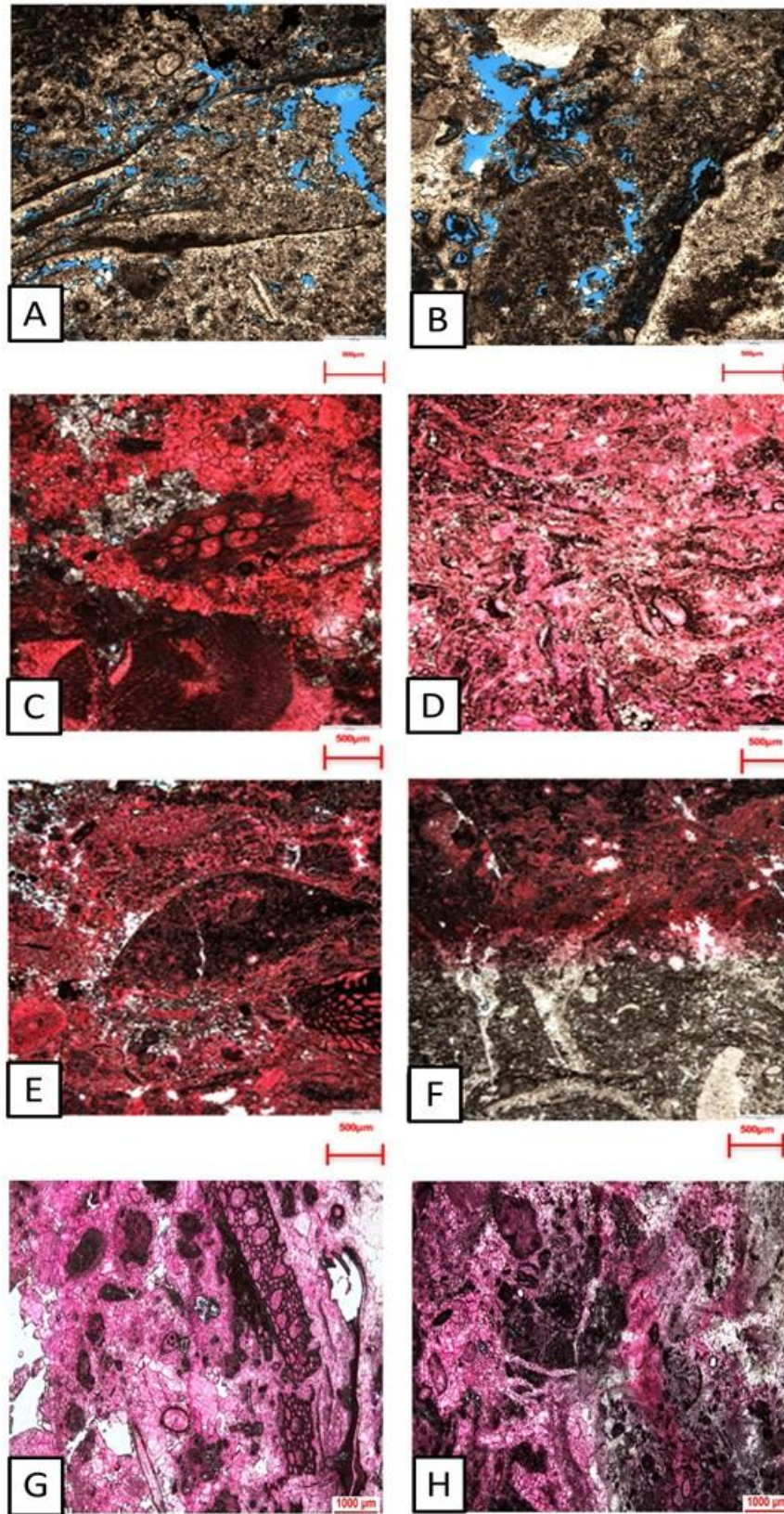


Figure 21

Figure 21: Photomicrographs of bioclast wackestone and packstone. Thin sections were stained with Alizarin Red-S solution. (A) & (B) Sparitic microbial bioclast wackestone that were recrystallized, where major bioclasts are *Komia*, bryozoans, and brachiopods, from the New Dell #2 well. (C) Bioclast wackestone with fragments of bryozoans and *Komia*. (D) Bioclast wackestone from the Eliasville Caddo Unit #106 well, 3273.3 ft. (E) Slightly dolomitic bioclast wackestone from the Eliasville Caddo Unit #106 well, 3259.1 ft. (F) Bioclast wackestone with *Komia* and crinoid, from the Eliasville #106 well, 3259.1 ft. Only the upper half was stained with Alizarin Red-S solution. Photomicrograph courtesy of Qilong Fu. (G) Bioclast packstone showing fragments of bryozoans, *Komia*, and crinoid, from the Newell Dell #2 well, 3281.8 ft. (H) Bioclast packstone showing the fragments of *Komia* and fusulinids, from the Newell Dell #2 well, 3289.5 ft.

Allochems in bioclast lithofacies are normally poorly sorted, having been deposited in moderate-energy environments. This lithotype is not common in the Caddo Limestone. It normally accounts for less than 5% of all the lithofacies. Additionally, some bioclast lithofacies are slightly to moderately dolomitized. Dolomitization made this lithofacies less porous than the *Komia* lithofacies and phylloid-algal lithofacies. Thus, bioclast lithofacies are not as good at preserving hydrocarbons as *Komia* or phylloid-algal lithofacies.

Depositional-Environmental Interpretation

Three major depositional environments have been interpreted based on core observations and thin section analysis. They are: (1) carbonate mound cores, (2) carbonate mound flanks, and (3) inter-mound environments. Each lithofacies type corresponds to one or more types of depositional environment. Table 4-1 displays the relationships of lithofacies and interpreted depositional environments.

Table 2: Major lithofacies and interpreted depositional environments of the Caddo Limestone in the Stephens County, North-Central Texas.

Lithofacies	Composition	Depositional Environments
<i>Komia</i> wackestone and mud-dominated packstone	Major allochem: <i>Komia</i> Minor allochems: echinoderms, bryozoans, foraminifers, brachiopods, ostracods, mollusks, phylloid algae	Carbonate mound cores
Phylloid-algal wackestone and packstone	Major allochem: phylloid algae Minor allochems: <i>Komia</i> , brachiopods, echinoderms, foraminifers, brachiopods, ostracods, bryozoans	Carbonate mounds, especially flanks
<i>Komia</i> grainstone and grain-dominated packstone	<i>Komia</i> and echinoderms with some fusulinids and crinoids	Intermound
<i>Komia</i> boundstone	<i>Komia</i> in vertical growth position	Carbonate bumps near mound flank
Bioclast wackestone to packstone	Allochems: <i>Komia</i> and bryozoans, brachiopods, echinoderms and possible mollusks. Intensely recrystallized	Intermound (slightly deep water)

Komia wackestone and mud-dominated packstone are distributed across the entire mound. First, *Komia*, the most common reef and mound builder, is recorded to be deposited in shallow water and moderate-to-low energy settings. Additionally, the presence of shallow-marine fossils such as miliolid foraminifers in this lithofacies indicates low-energy environments of deposition (Nakasawa et al., 2009).

Carbonate mound flanks are generally associated with phylloid-algal wackestone and packstone. After the stabilization of the hard-substrate surface, the mound grew and large quantities of sediments accumulated. The initial growth of phylloid algae was slow on the hard substrate, yet once established, the organisms started growing rapidly due to their high reproduction rates (Toomey, 1980). Phylloid algae could not survive without continuous provision of light. Mound flanks initially provided an ideal condition for the phylloid algae to thrive, and the algae consequently kept the mound core within the photic zone owing to their rapid growth and baffling effects. Thus, phylloid algae became the dominant flora of the photic areas at the mound (Wilson, 1975). Phylloid algae blades were delicate, which indicated low-energy settings, and the large-bladed phylloid rocks represent a quieter water environment, where large blade pieces of algae settled to the mound with little or no agitation (Miller, 2001). These whole blades had some rigidity when they were settled and the original porosity that later was filled with mosaic calcite can be observed (Wilson, 1975). The algal blades trapped carbonate mud and deposited it near the base of the plant. The mound core grew upward mostly below normal wave base with addition of accommodation space. Some storm waves would have broken large blades of phylloid algae and transported some minor skeletal grains such as foraminifers and gastropods (Heckel and cocke, 1969).

Inter-mound environments normally form in the central portion of the algal mound complexes between mound tops (Chidsey et al., 1996). The lithofacies associated with the inter-mound depositional environment is bioclast wackestone. Skeletal grains, such as *Komia*, brachiopods, bryozoans, and phylloid algae, broke apart and either washed in from the carbonate mounds or they originally grew in the inter-mound regions. Many allochems, which are small fragments or broken into pieces, show strong evidence of being transported from elsewhere. Other grains, relatively larger and more complete, were produced locally in the habitats by the living organism (Miller, 2001). *Komia* grain-dominated packstone and grainstone are also found in the inter-mound regions. It indicates moderately high energy settings. This lithofacies contains diverse large skeletal grains shed off from the mound core. Grains may include fusulinids, ostracods, brachiopod spines, bryozoans, *Komia* fragments, crinoids, and phylloid algal chips. Varying carbonate mud amount, different particle sizes, different skeletal types, and a range of textures from packstone to grainstone are produced based on the distance of transport away from the mound complexes. The transportation of skeletal grains produces extremely battered grains that show some signs of fragmentation, abrasion and brecciation (Miller, 2001), which are more obviously visible in the core samples of *Komia* grain-dominated packstone and grainstone than are the samples of other lithotypes.

The carbonate environments near the flank are mostly associated with *Komia* boundstones. Skeletal grains at this depositional environment were either transported a short distance or were originally deposited there. *Komia* thallus trapped carbonate mud and other particles that served as an effective baffle to moderate waves and currents. Skeletal grains are usually complete in shape and show only slightly abrasion or fragmentation due to an absence of high-energy waves.

In Cycle A of the Caddo Formation, *Komia* lithofacies (packstone and wackestone) are widely spread (Fu et al., 2017), and mainly distributed in the middle and upper interval of Cycle A. Phylloid algal lithofacies are minor, and mainly restricted to the lower and middle interval of Cycle A. The distribution of these two lithofacies is controlled in part by water depth and energy level. *Komia* beds have been interpreted as occupying shallow to moderately deep shelf environments, flanking to topping phylloid-algal mounds or occurring in topographic highs on the seafloor (Wahlman, 2002). Previous studies suggested that phylloid algae likely-lived below wave base and could have thrived in water depths of around 100 ft (Roberts et al., 1987, Soreghan and Giles, 1999). In addition, *Komia* lithofacies may show graded bedding and rare cross-stratification that were not observed in phylloid-algal lithofacies. Phylloid-algal lithofacies contain abundant mud with little evidence of strong wave or current agitation. Phylloid algae always occur in cores as fragments, whereas *Komia* are occasionally found *in-situ* with intact delicate networks of branches.

Komia lithofacies are dominant in the Eliasville Field, and much more abundant than in nearby Curry, Park and Breckenridge Fields (Weber, 1995; Miller, 2001; Entzminger et al., 2012). This is interpreted to be related to the paleographic locations of these fields. As the paleographic map suggests (Figure 2-1), the Eliasville Field was probably located at or closer to the shelf margin in a high energy setting where phylloid algae were less likely to thrive.

Geological Modelling

Well Logs and an Artificial Neural Network

An artificial neural network (ANN) was applied to study two cored wells with the best data set and the most complete well log data. With their core information and well logs, the selected wells conducted mutual-learning and summarized regularities from that.

In this study, a back-propagation algorithm was applied in the geological artificial neural network system.

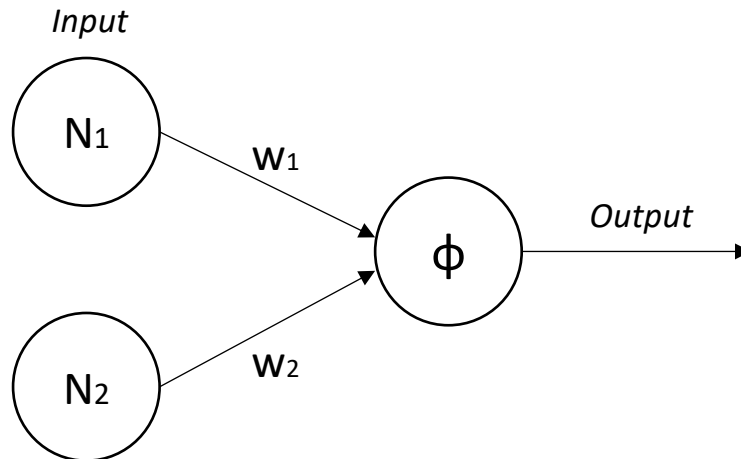


Figure 22: Simplified diagram of a back-propagation artificial neural network

In a back-propagation artificial neural network (Bp-ANN), N_1 and N_2 represent two inputs. The final output is generated by a linearly weighted sum of all its input. The diagram is shown as below, where w_1 and w_2 are the weights of N_1 and N_2 , respectively (Pradhan and Lee, 2010).

The output of the system is usually not the expected value and when the error exists, back-propagation stimulates the system to re-conduct the training to decrease the value of error E (Dedecker et al., 2004). The smaller the error is, the more accurate the output will be (Gardner and Dorling, 1998).

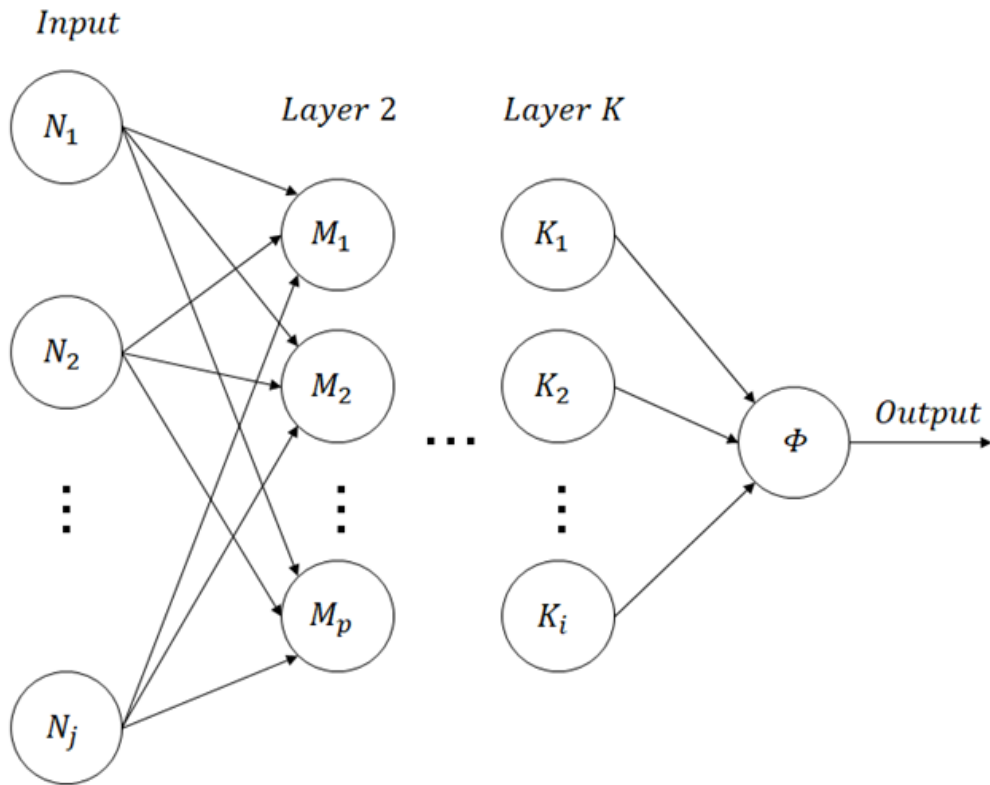


Figure 23: Demonstration of an integrated ANN system with multiple inputs and various layers

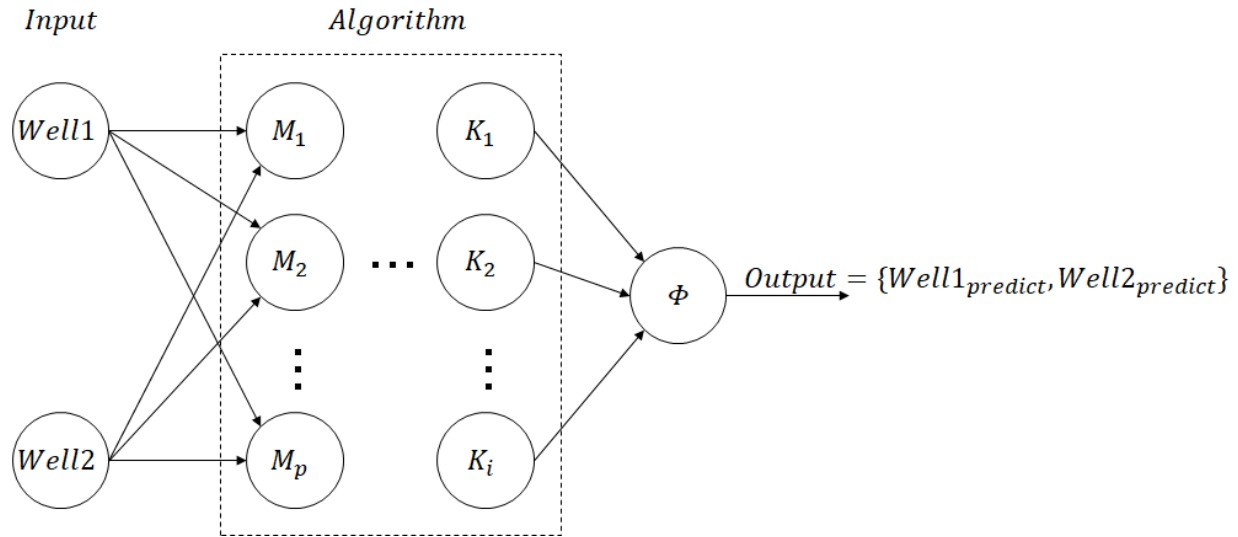


Figure 24: Demonstration of the artificial neural network where the input is data from two wells and the output is the predicted lithofacies distribution in these two wells

The input in this ANN is the set of wireline logs and core description of Well1 and Well2, where the wireline logs include the curves of GR, RHOB, ILD, ILM, PHIT and PHIE (Qi and Carr, 2006).

$$\text{Well1} = \{\text{Lithofacies1}, \text{WirelineLogs1}\}$$

$$\text{Well2} = \{\text{Lithofacies2}, \text{WirelineLogs2}\}$$

By applying different numbers of iterations, limiting errors and establishing a probability threshold, one can get the output of predicted lithofacies distribution of both Well1 and Well2.

$$\text{Output} = \{\text{Lithofacies1}_{\text{predict}}, \text{Lithofacies2}_{\text{predict}}\}$$

Well Correlation by Cores

Carbonate reservoirs are more heterogeneous than are siliciclastic reservoirs, which makes carbonate reservoir characterizations more difficult (Yose et al., 2006). Additionally, wireline logs do not correspond closely to the lithofacies of carbonate rocks. Therefore, cores are normally applied to well correlation. The artificial neural network (ANN) was applied in well-core correlation. Eliasville Caddo Unit #33 and East Eliasville Caddo Unit #46 are the two sample wells, sites of mutual-learning and replicating each lithofacies distribution on well logs. The input of this ANN system is the real core data, represented by L33-A and L46-A in the figure, and six wireline curves, which are gamma-ray (GR), density curves (RHOB), deep induction resistivity logs (ILD), medium induction resistivity logs (ILM), total porosity curves (PHIT), and effective porosity curves (PHIE). The output is the predicted lithofacies of these two wells. Theoretically, if the predicted versions of lithofacies distribution are 100% the same as those of the cores, the algorithm of this artificial neural network is proved to be effective for the model. However, it is normally impossible to duplicate the reality. Practically, if the predicted version of lithofacies resembles to a high extent their real core descriptions (the error E is tolerable and smaller than a given value), the simulation proved to be successful. As a result, when the iteration times of back-propagation cycles are set at 2000 and the error limit is set at 10, the output, denoted by L33-B and L46-B, resembles fairly well their real core data, as is demonstrated in Figure 5-4.

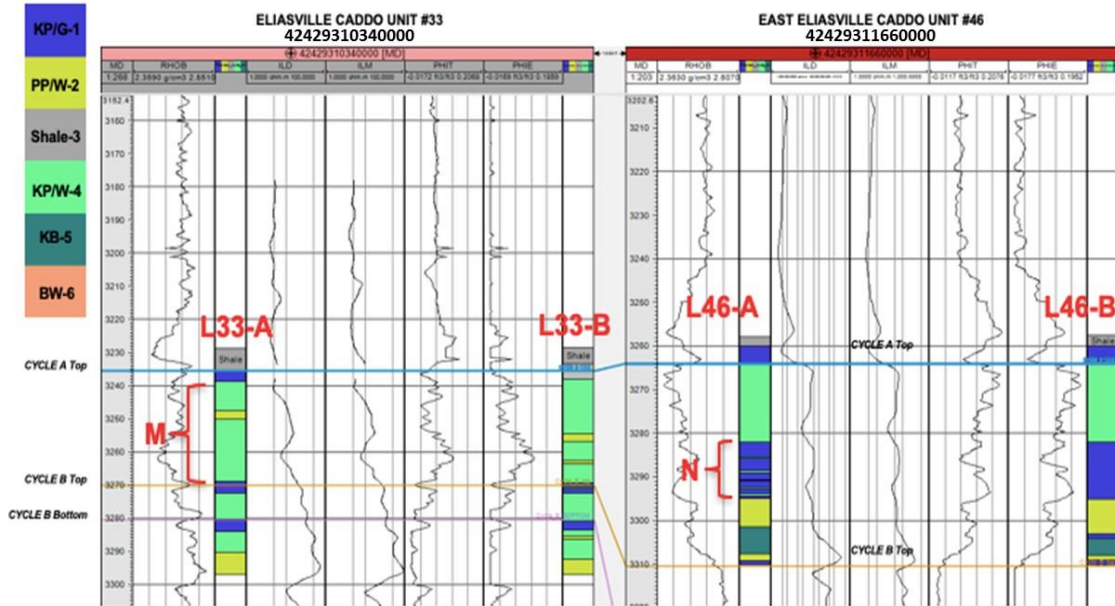


Figure 25: Well correlation and lithofacies simulation in the Eliasville Caddo Unit #33 well (left) and East Eliasville Caddo Unit #46 well (right).

L33-A and L46-A are both from the cores, which are compared with L33-B and L46B, which are the simulation results. By doing the comparison, several features of this algorithm are clear. First, all the lithofacies appearing in the cores are simulated through ANN. Secondly, the thickness of the intervals in L33-A and L46-A are approximately equivalent to that of L33-B and L46B.

However, there are also some defects in this simulation. The first is that the depth of a certain type of lithofacies might vary in the predicted lithofacies distribution, as exemplified by interval M in L33-A and its corresponding interval in L33-B. In L33-B, phylloid algal wackestone and packstone, indicated in yellow, appears to be lower than expected. Another obvious defect is illustrated by interval N in L46-A and its corresponding interval in L46-B. There are a few beddings of *Komia* wackestone and mud-dominated packstone within the lithofacies of *Komia* grainstone and grain-dominated packstone. These beds are thin, having a thickness of less than 1 ft.

Results are also supposed to run the testing by other cored wells to prove that this methodology is effective for the whole study area.

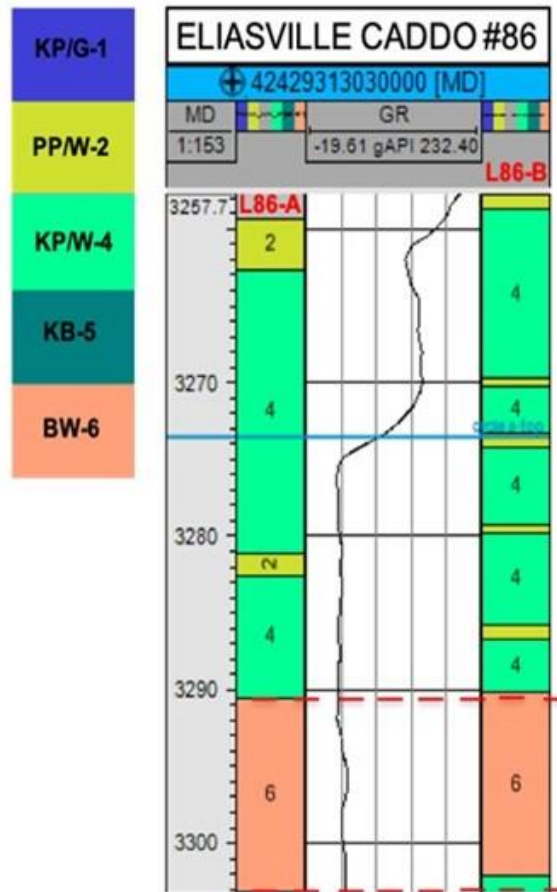


Figure 26: Lithofacies distribution of the Eliasville Caddo #86 well, from both core description (L86-A) and the artificial neural network's simulation (L86-B).

In the core from the Eliasville Caddo #86 well, three lithofacies are distinguished: (1) phylloid-algal packstone and wackestone, (2) *Komia* wackestone and mud-dominated packstone, and (3) bioclast wackestone. Two intervals of *Komia* wackestone and packstone have thicknesses of 18.3 ft and 7.9 ft with a total of 26.2 ft. The thicknesses of two intervals of phylloid-algal wackestone and packstone are, respectively, 3.4 ft and 1.5 ft, for a total of 4.9 ft. The third type of lithofacies, bioclast wackestone, has a thickness of 12.5 feet. The simulation in L86-B has the best result for bioclast wackestone, which has a thickness of 12.1 ft. The error for this lithofacies in

terms of thickness is 3.2% and the depth is 0.4 ft moved upward only (demonstrated between two red dashed lines; Figure 4-17). The total thickness simulated for phylloid-algal wackstone and packstone is 4.1 ft, and compared to the 4.9 ft in the core, the error is 16.3%. Instead of only two intervals of this lithofacies, five intervals of this type show up in L86-B. Similarly, *Komia* wackestone and mud-dominated packstone, has a thickness of 28.6 ft, compared to 26.3 ft in the core. The error percentile is 8.7%.

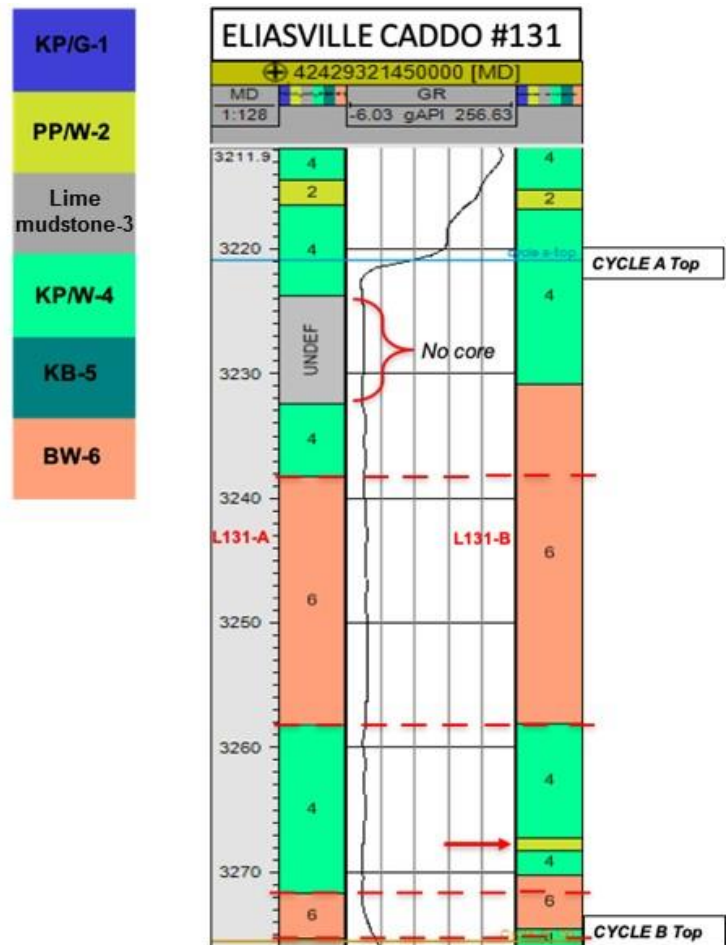


Figure 27: Lithofacies distribution of the Eliasville Caddo #131 well, from both core description (L131-A) and the artificial neural network's simulation (L131-B).

The Eliasville Caddo #131 well is another cored well yet it lacks complete core data. In the uppermost part of the well, there is an undefined part with no core data. This part is approximately

8.7 ft. In L131-B, the corresponding depth is recovered by *Komia* wackestone and mud-dominated packstone. The thickness of the bioclast wackestone is larger than expected, and the depth is elevated compared to that in L131-A. Phylloid-algal wackestone and packstone is 1.9 ft in L131-A, but, in L131-B, it has been divided into two parts and the in total thickness is 2.1 ft. This error can be tolerated.

Lithofacies Distribution

The surface of the distribution model was build up based on 3-D seismic data. The wells were tied to the seismic too. A total of 586552 geocellular grids with a size of 483*506*24 inches were constructed in this three dimensional model. Kriging algorithm was applied in the process of modelling. The lithofacies were tied to the well logs and then propagated to each cell.

A lithofacies distribution map was constructed on the basis of a geologic structure map. The complete lithofacies map of Cycle-A and Cycle-B is shown as Figure 5-7. Two enlarged maps of some detailed geologic structures will also be demonstrated. In the lithofacies map, both mound features and lithofacies distribution can be observed. Five lithofacies demonstrated in the lithofacies map of Cycle A, each color representing a lithofacies type.

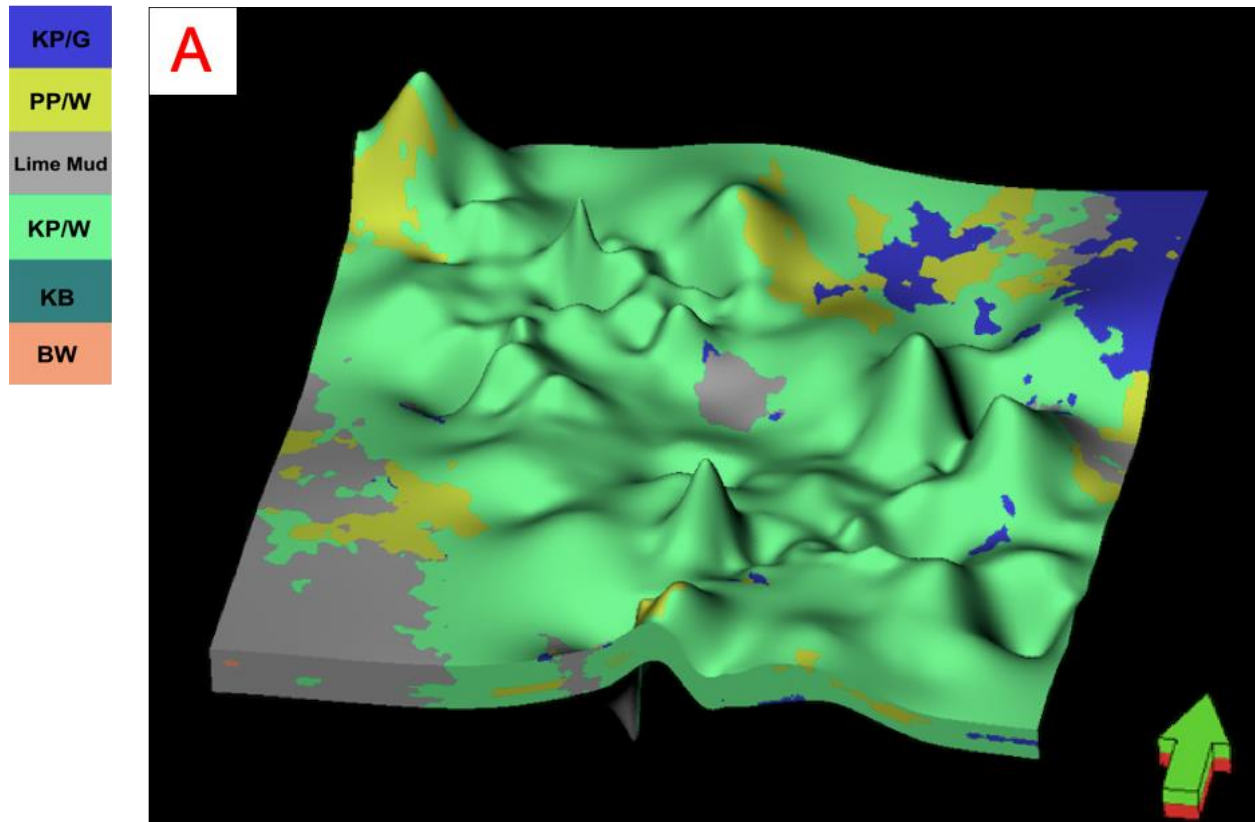


Figure 28: 3-D lithofacies distribution map of Cycle A. *Komia* grainstone and grain-dominated packstone is indicated in blue. Phylloid-algal wackestone and packstone is indicated in yellow. *Komia* wackestone and mud-dominated packstone is indicated in green. *Komia* boundstone is indicated in indigo. The bioclast wackestone is indicated in pinkish red, and the lime mud/shale is represented in gray.

In Figure 5-7, it is observable that carbonate mounds are generally composed of *Komia* wackestone and mud-dominated packstone, as well as phylloid-algal wackestone and packstone. *Komia* wackestone and mud-dominated packstone is the predominant lithotype in the Cycle A. Phylloid-algal lithofacies is abundant at mound flanks, due to a sufficient sun-light supply there. This type of algae is also associated with macropores and vuggy pores, hence they can host hydrocarbons. Therefore, mound cores might often exist where the hydrocarbons reside.

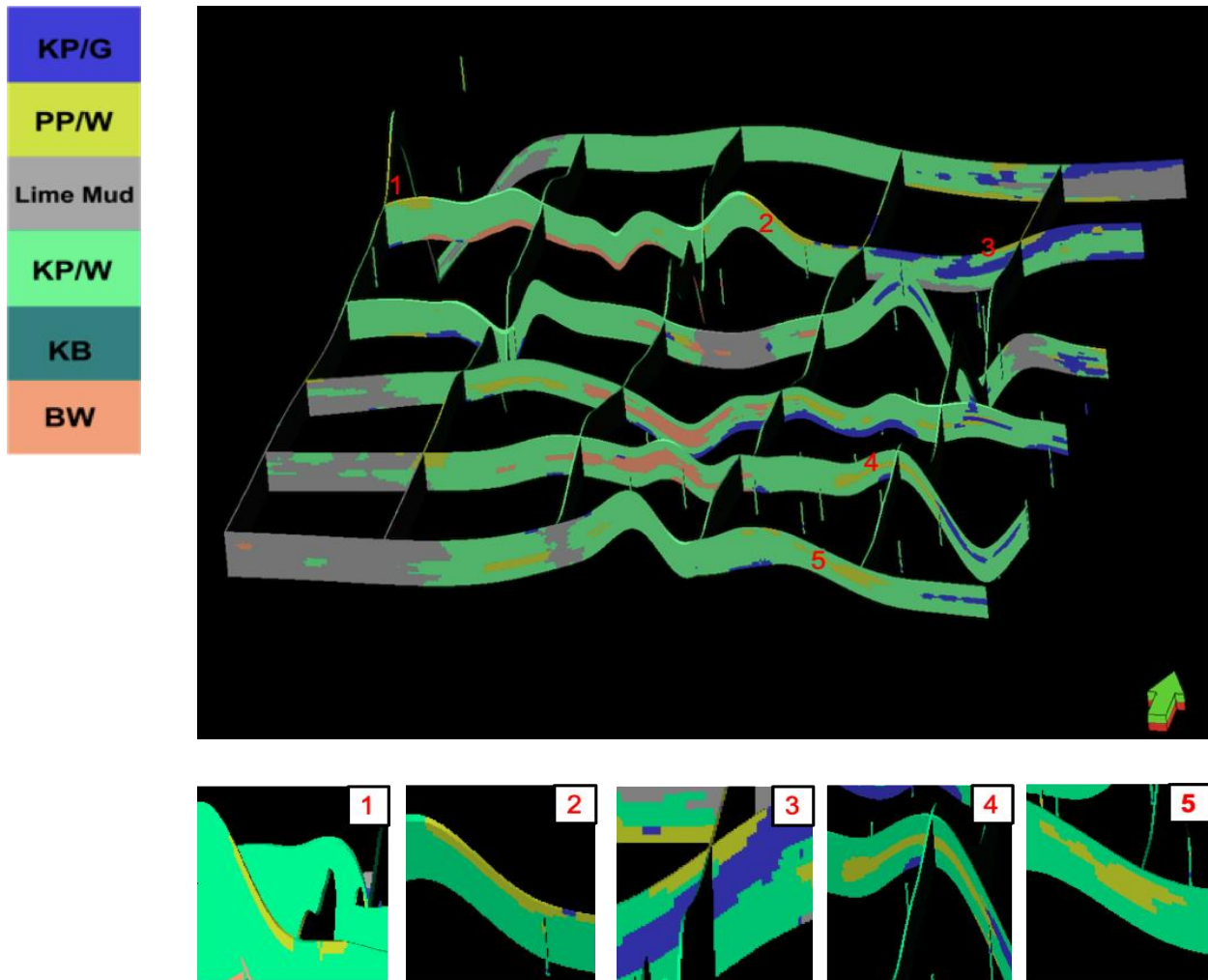


Figure 29: Fence diagram of Cycle A, showing the lithofacies distribution within the architecture, with an enlarged diagram of 1-5 displaying phylloid-algal wackestone and packstone.

Phylloid algae are observed to be abundant in the carbonate flanks, which are the photic zones at the Caddo Limestone. The energy level of carbonate core is comparatively low to moderate. Without high-energy flow such as waves or tides, phylloid algae were not transported from the mound flanks farther away. When lime mud was transported to the carbonate flanks, most of it was trapped by phylloid algae due to the baffling effects of the algae blades. Grains shed off from the mound core were transported further away by the energy flow and are more likely to accumulate between two groups of carbonate mounds or north eastward at the eastern edge of the Concho Platform, where *Komia* grain-dominant packstone and grainstone was mostly deposited.

Thereby, based on the cores and thin sections, as well as lithofacies distribution associated with various porosity types, it can be known that from the southwestern to the northeastern parts of the study area, there may be a very general trend for the grain size to get larger and coarser.

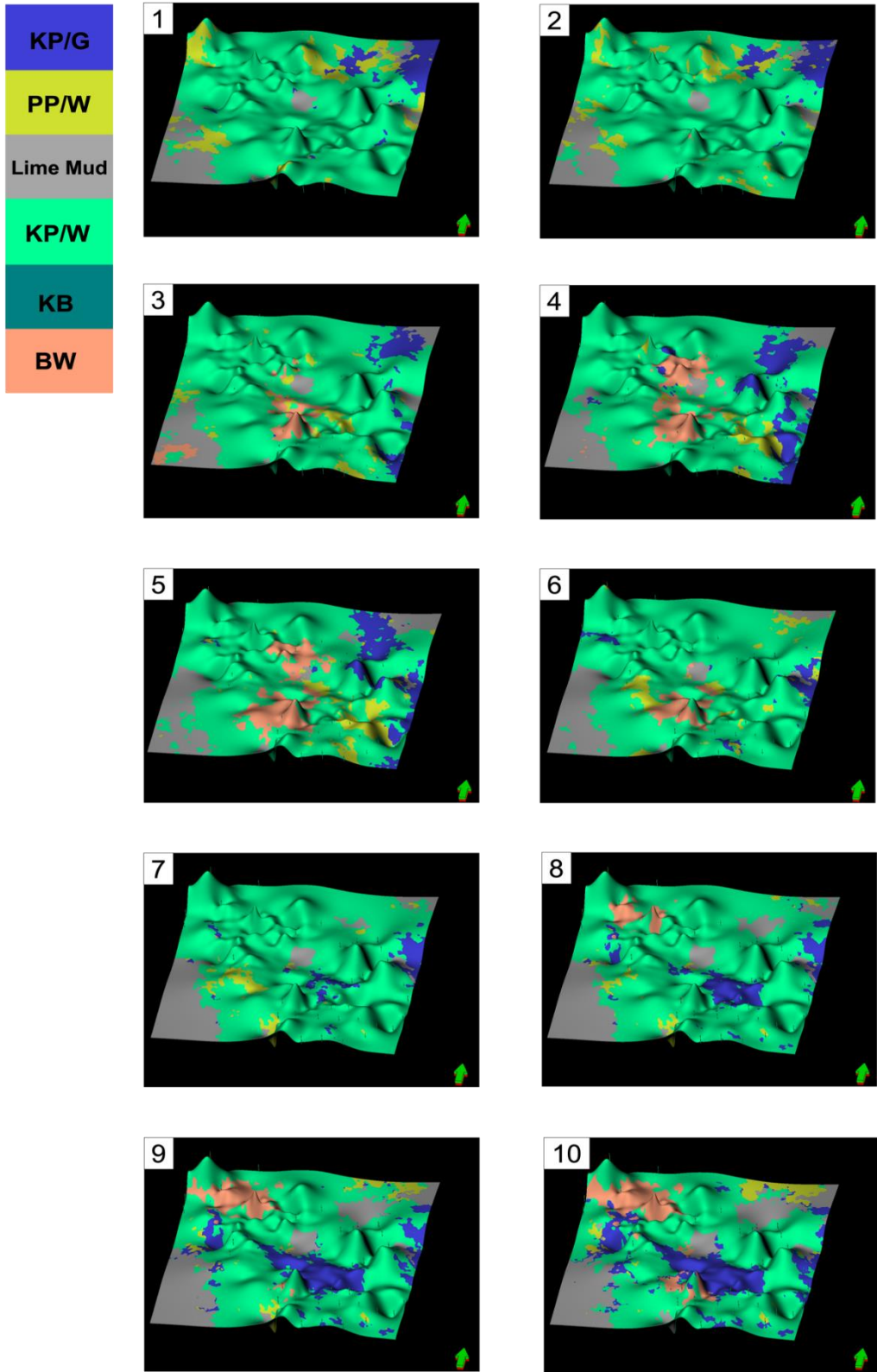


Figure 30: Ten surfaces, 1-10, sampled from the 3-D facies map of Cycle A, showing the vertical variation of lithofacies distribution with respect to the Z-axis.

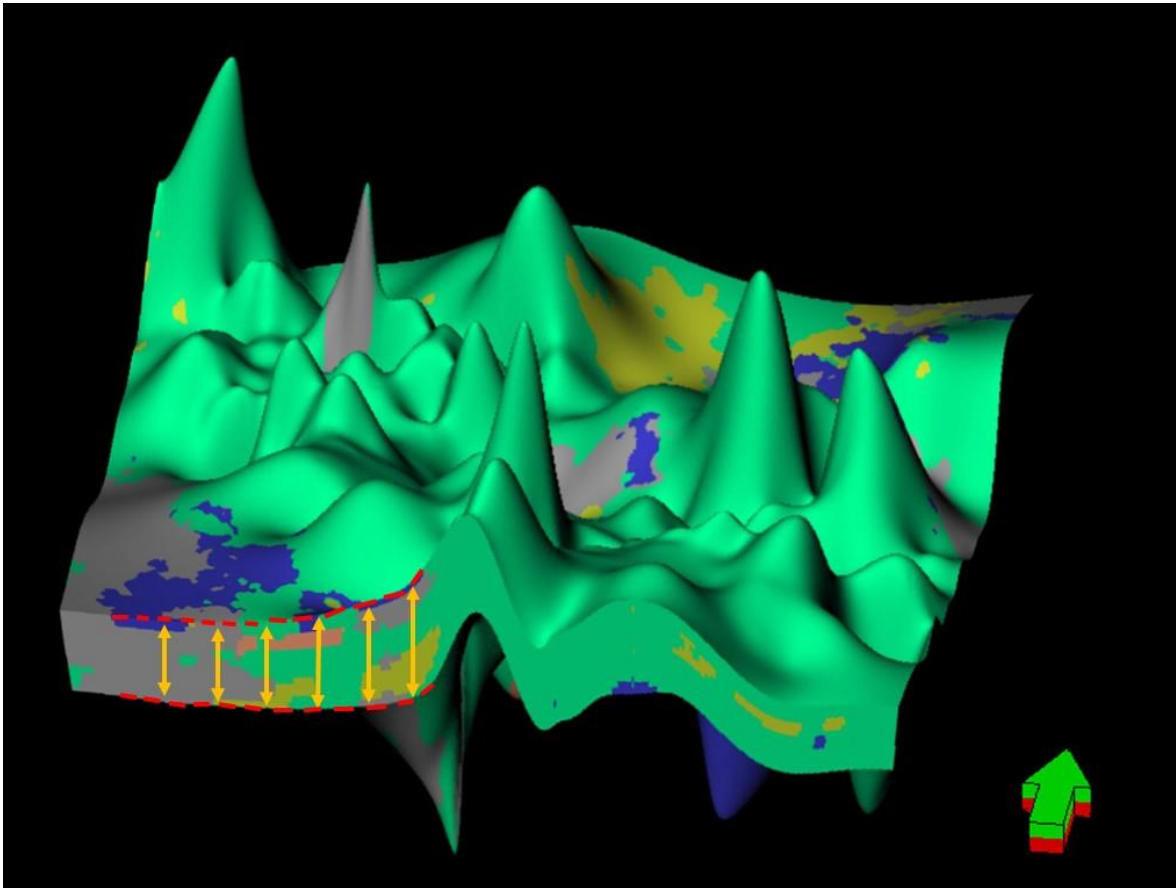


Figure 31. A 3-dimensional lithofacies model of the Cycle A with the Z scale set to be 50. Red dashed lines and orange arrows indicate the thickness trend from non-mound region to mounds.

Figure 5-10 demonstrates that the mound has a slightly larger thickness than intermounds or flanks, thereby indicating potentials for hydrocarbon reserves. Cycle A has a thickness range of 10 ft to 65 ft. Ten surfaces have been sampled, and the distance between two adjacent surfaces ranges from 1.1 ft to 7.2 ft. The sampled surfaces demonstrate a vertical variation pattern of the lithofacies distribution. *Komia* wackestone and mud-dominated packstone is a predominant type of lithofacies in the Cycle A, especially in the upper half of this cycle. Phylloid-algal wackestone and packstone is normally found to be a slightly more abundant in the uppermost of the Cycle-A, as can be observed from surfaces 1-6 in Figure 5-9, at the topographic high locations. By comparison, bioclast wackestone was mainly deposited in the lowermost part of Cycle A, as seen from Figures

5-9-3 to Figure 5-9-10. The grains in the *Komia* wackestone are more various and poorly sorted than the phylloid-algal lithofacies. *Komia* wackestone (Figures 5-9-4 to Figure 5-9-10) is usually found at the locations between two mound tops. Some *Komia* are found to have been deposited at mound flanks or at small mound tops. *Komia* is mostly found at the high-energy settings on the Concho Platform. Influenced by the local tectonics, sediments shed off from two groups of carbonate mounds were transported northeastward (Hentz, et al., 2012), which generated two major locations of *Komia* grainstone and grain-dominated packstone deposition. The first location is the large inter-mound area between the two series of carbonate mounds. The second site is almost at the eastern edge of the Concho Platform, which is northeast of the outer carbonate mounds.

Cycle B has a thickness range of 0 to 40 ft, which is much thinner than the Cycle A. The lithofacies distribution of Cycle B is very different from that of Cycle A as well. Because it has fewer phylloid-algal lithofacies and effective pores, Cycle B is not a good hydrocarbon reservoir compared to Cycle A.

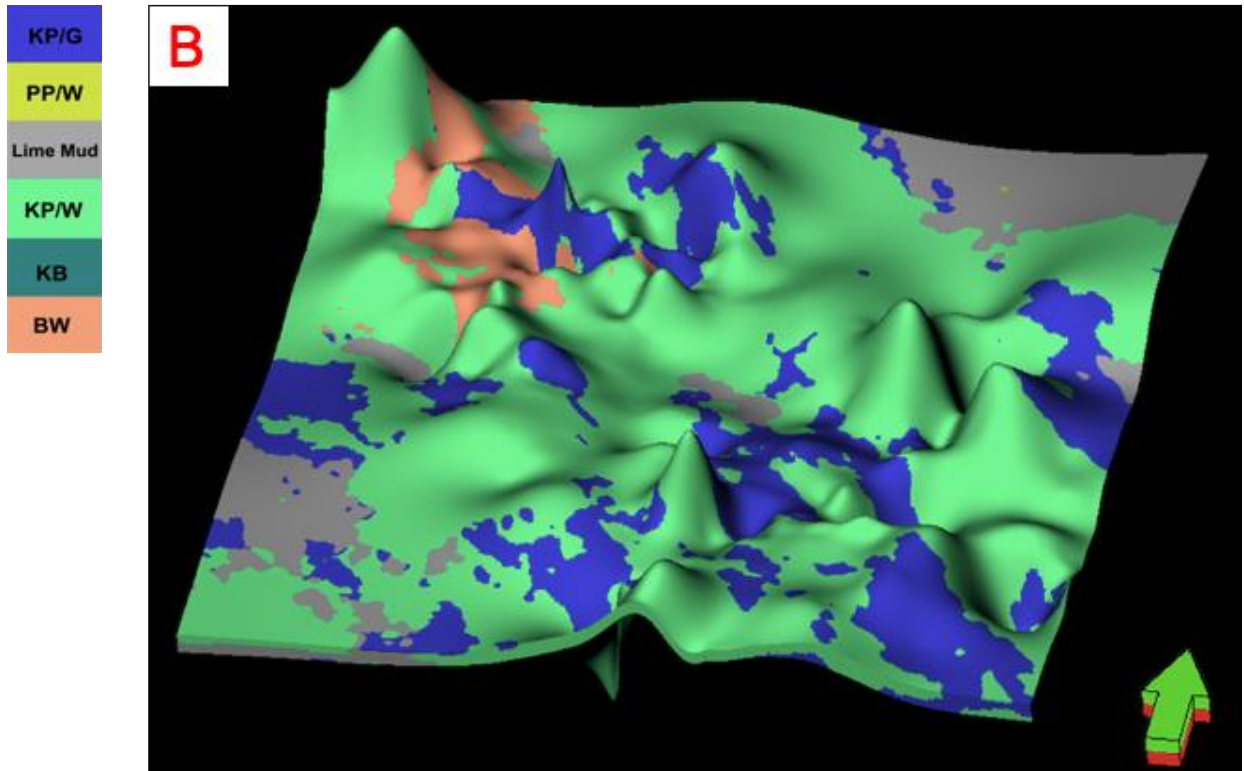


Figure 32: A 3-D lithofacies distribution map of Cycle B. *Komia* grainstone and grain-dominated packstone are indicated in blue, Phylloid-algal wackstone and packstone are indicated in yellow, *Komia* wackestone and mud-dominated packstone are indicated in green, *Komia* boundstone is indicated in indigo, the bioclast wackestone is indicated in the pinkish red, and the lime mud/shale is represented in grey.

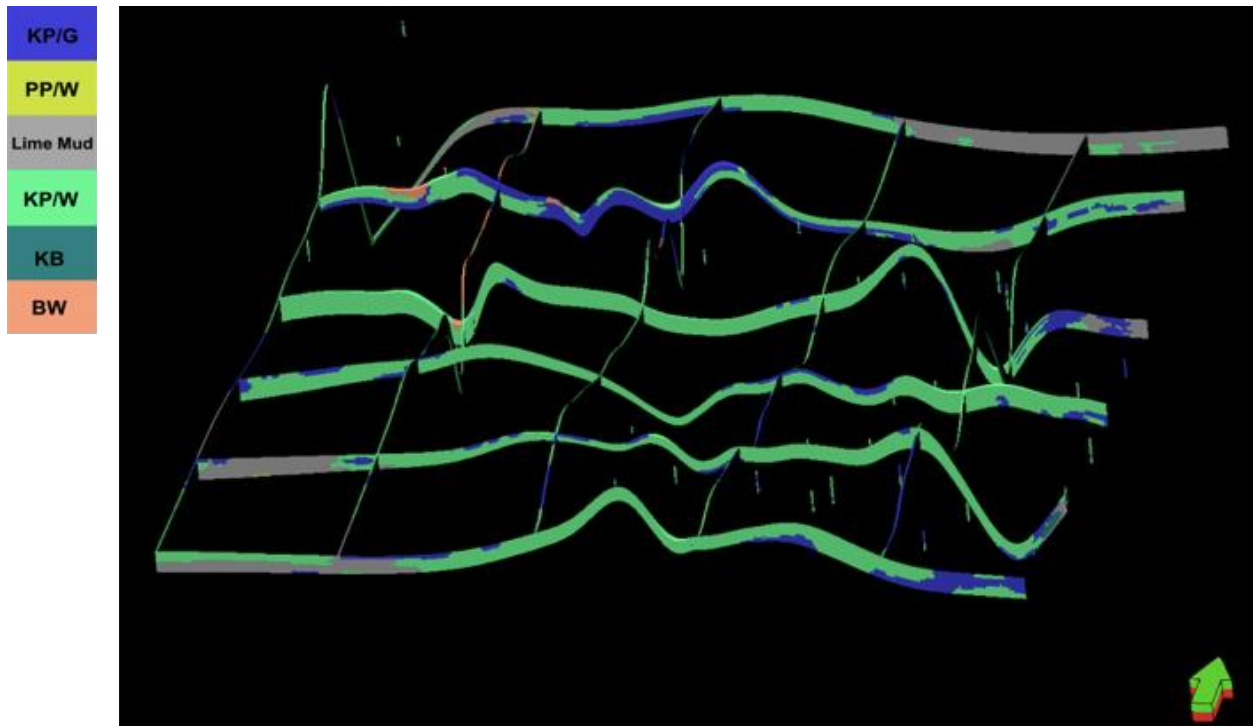


Figure 33: Fence diagram of Cycle B showing the lithofacies distribution within the architecture.

Based on the facies map and fence diagram of Cycle B, fewer types of lithofacies are shown in this interval. The predominant lithofacies in Cycle B is still *Komia* wackestone and mud-dominated packstone. *Komia* grainstone and grain-dominated packstone also takes up a large proportion of Cycle B. However, *Komia* boundstone and phylloid-algal lithofacies are not visible in this cycle.

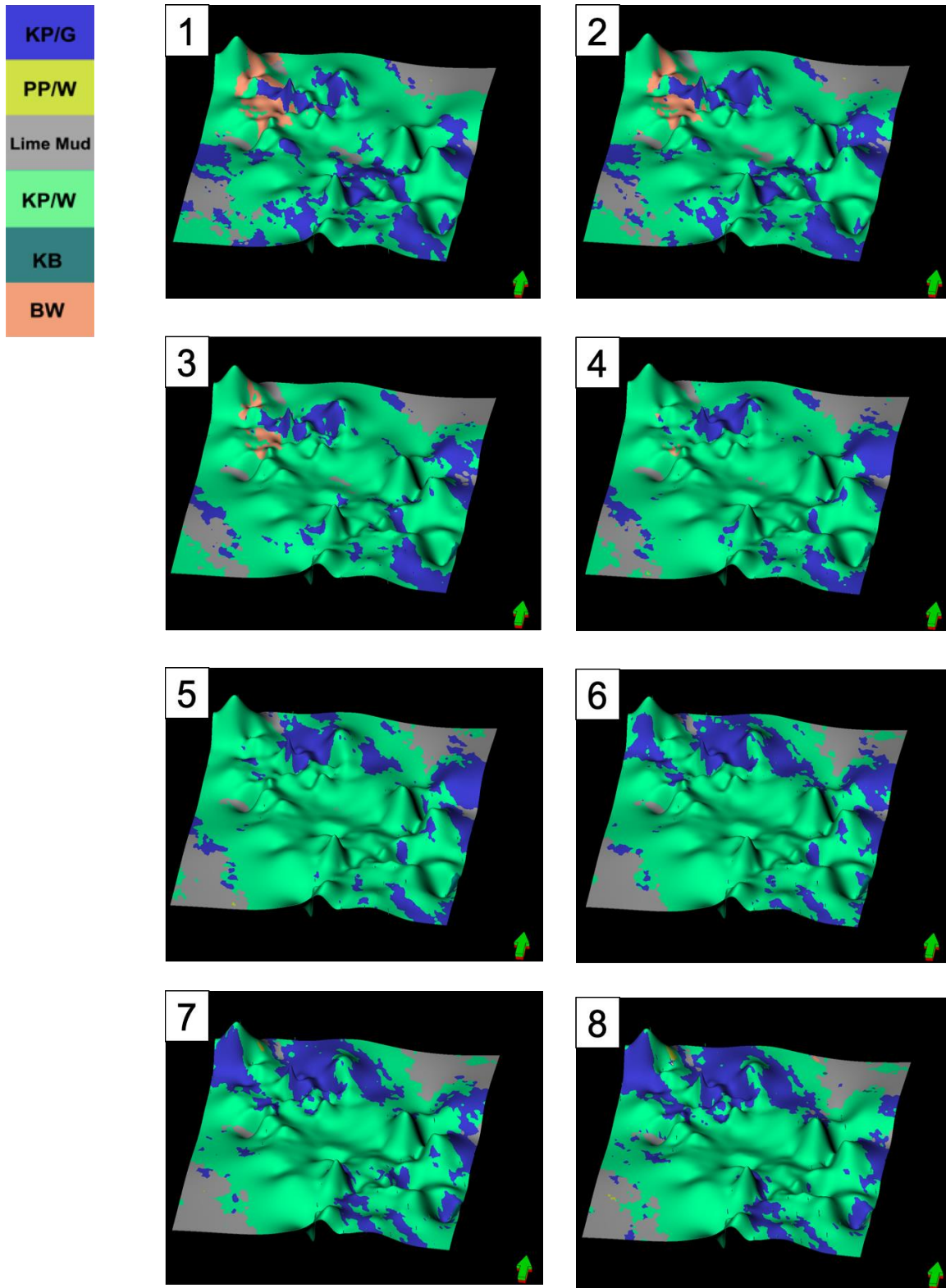


Figure 34: Eight surfaces sampled from the 3-D facies map of Cycle B, showing the vertical variation of lithofacies distribution with respect to the Z-axis.

Eight surfaces have been sampled from the top to the bottom of Cycle. Bioclast wackestone is less in Cycle B than in Cycle A. Additionally, bioclast wackestone is only found to be deposited in the upper part of the Cycle B, as can be viewed from Figures 5-13-1 to Figure 5-13-4. The deeper the surface, the less bioclast wackestone can be observed. *Komia* grainstone and grain-dominated packstone, in contrast, are distributed almost evenly along the Z-axis. Most of the deposition took place in the northwestern and southeastern areas of the Caddo Limestone, near the carbonate mound flanks. Cycle B is a moderately high energy setting, which is not an ideal condition for the deposition of phylloid algae, thus, such allochems are not found deposited in Cycle B. *Komia* boundstone, which is associated with carbonate bumps, does not take place here either.

Statistical and Component Analysis

Based on the variogram and principal component analysis, the probability model of the lithofacies map is optimized and the percentile of each lithofacies can be calculated (Khatriwada et al., 2013). Compared to the qualitative conclusion acquired from core description and thin section analysis, major components of each cycle can be revealed in a quantitative method.

Table 3: Proportion of five lithofacies types in Cycle A, acquired from *Petrel*.

Lithofacies Type	(%) Percentile
<i>Komia</i> grain-dominated packstone and grainstone	9.08
Phylloid-algal wackestone and packstone	6.85
<i>Komia</i> wackestone and mud-dominated packstone	81.06
<i>Komia</i> boundstone	0.1
Bioclast wackestone	2.91

Table 4: Proportion of five lithofacies types in Cycle B, acquired from *Petrel*.

Lithofacies Type	(%) Percentile
<i>Komia</i> grain-dominated packstone and grainstone	24.32
Phylloid-algal wackestone and packstone	0.34
<i>Komia</i> wackestone and mud-dominated packstone	73.31
<i>Komia</i> boundstone	1.01
Bioclast wackestone	1.01

Table 5-1 and Table 5-2 provide several results. In both Cycle A and Cycle B, *Komia* wackestone and mud-dominated packstone is the only predominant lithotype, being 81.06% and 73.31% respectively. *Komia* grain-dominated packstone and grainstone is the second most abundant, at 9.08% of Cycle A and 24.32% of Cycle B. Thereby, total *Komia* lithofacies account for approximately 90% of Cycle A and 97% of Cycle B.

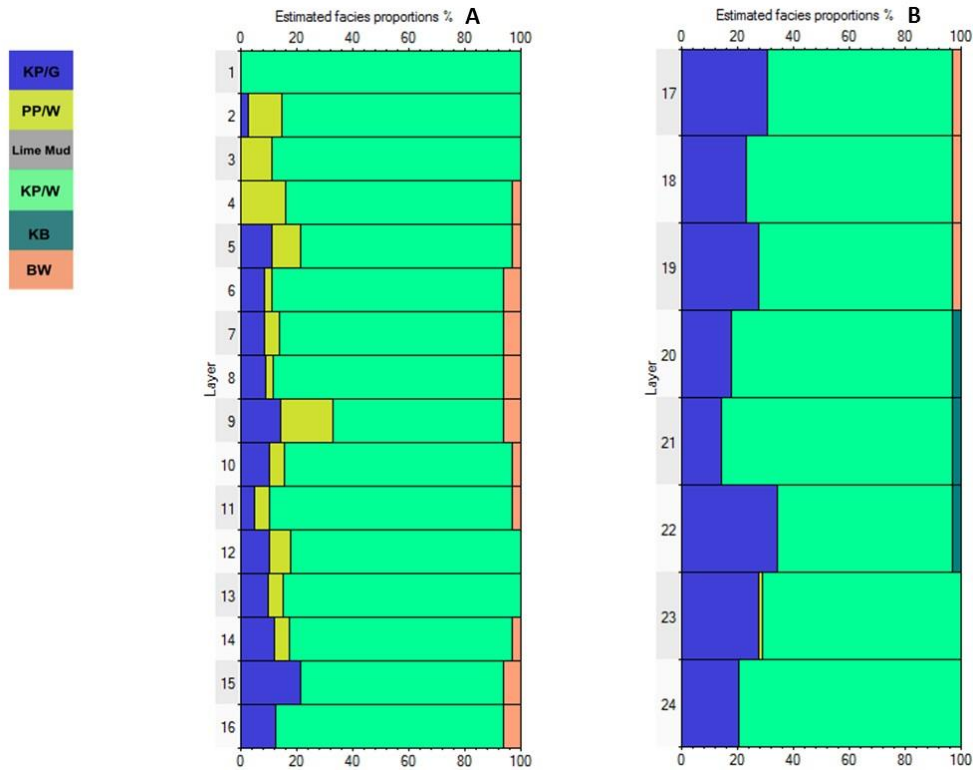


Figure 35. Estimated facies proportions and vertical distribution in both Cycle A and Cycle B

There are two types of lithofacies that are significantly more abundant in Cycle A than in Cycle B. The first is phylloid algae wackestone and packstone, which accounts for 6.85% of Cycle A, compared to only 0.34% of Cycle B. The other lithotype is bioclast wackestone, composing approximately 3% in Cycle A and 1% in Cycle B. *Komia* boundstone is found insignificant in both Cycle A and Cycle B, accounting for less than 1% in both cycles.

Table 5: Composite footage of five lithofacies types in Cycle A, acquired from core samples.

Lithofacies Type	Total Length (feet)
<i>Komia</i> grain-dominated packstone and grainstone	85
Phylloid-algal wackestone and packstone	57.2
<i>Komia</i> wackestone and mud-dominated packstone	533.6
<i>Komia</i> boundstone	4.9
Bioclast wackestone	19.3

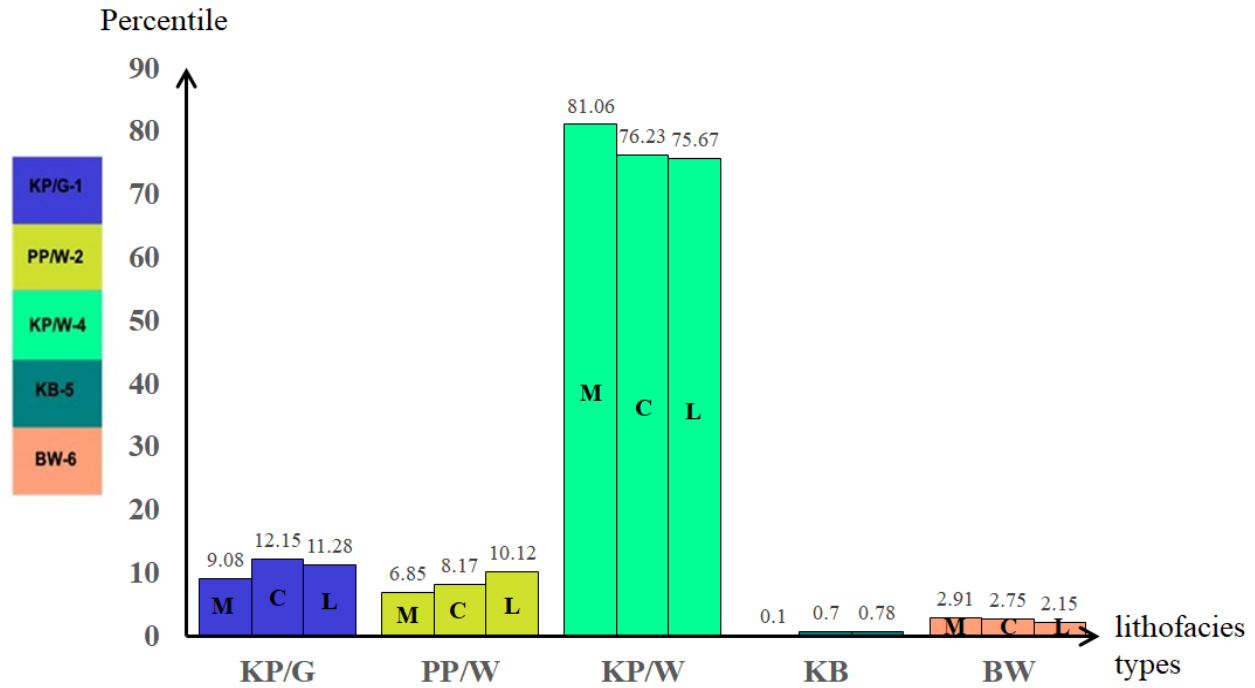


Figure 36. Facies proportions of Cycle A, KP/G = *Komia* grain-dominated packstone and grainstone, PP/W = Phylloid-algal wackestone and packstone, KP/W = *Komia* wackestone and mud-dominated packstone, KB = *Komia* boundstone and BW = Bioclast wackestone. The M columns represent facies proportions of the model, C columns represent facies proportions of the core samples, and L columns represent facies proportions from the well logs.

The proportionality of the various lithofacies types is generally the same in the model, the cores, and the wireline logs. *Komia* boundstone is extremely poorly represented in all three datasets: 0.1% in the model, 0.7% in the core samples, and 0.78% in the well logs. This apparent discrepancy resulted from the low simulation rate of *Komia* boundstone by the back-propagation algorithm. Some *Komia* boundstones are simulated as *Komia* wackestone and mud-dominated packstone in the model.

Discussion

Cycle A and Cycle B at the top of the Caddo Limestone are interpreted to be deposited in the algal mound and other mound-related environments. Based on the thin section analysis and core descriptions, each lithofacies is observed to be associated with depositional environments having different energy levels.

At the Caddo Limestone, *Komia* wackestone and mud-dominated packstone is found to be widely distributed in both Cycle A and Cycle B, either above or below the wave. *Komia* wackestone and mud-dominated packstone takes up 70% of the full length, which is approximately 600 ft. Apart from *Komia*, the occurrence of bryozoans, echinoderms, ostracodes, mollusks and brachiopods also indicates normal marine condition, which is further proved by the poor sorting, abundant matrix, and lack of mechanical stratification (Fu & Ambrose, 2017).

The phylloid-algal lithofacies is composed of complete phylloid algae blades. At the Caddo Limestone, phylloid algae are found mostly away from the waves and tides. Comparatively, *Komia* wackestone and mud-dominated packstone are also deposited in the low-energy environments, yet they might be moderately higher than in the energy settings corresponding to phylloid algae. In general, *Komia* wackestone and packstone is found to be at shallow to moderately-deep shelfal environments. Bioclast wackestone and packstone, with more kinds of skeletal grains, worse sorting, and less carbonate mud, is deposited in higher energy settings than *Komia* wackestone and mud-dominated packstone. The color of bioclast wackestone varies greatly, from the dark colors (rich in organics) to light gray. Bioclast wackestone and packstone is usually found in slightly deep water with moderate energy level. *Komia* grainstone and grain-dominated packstone has no carbonate mud and is the most abundant in grains. Most of the grains were transported by moderate- to high-energy flows to the locations where they were deposited.

Based on the sequence of energy level associated with each lithofacies, Cycle A is a lower energy setting than Cycle B. First, Cycle B contains almost no phylloid-algal lithofacies and less bioclast wackstone, which indicates low-energy environments. Second, although both Cycle A and Cycle B are composed of *Komia* grainstone and grain-dominated packstone as the second most abundant type of lithofacies, Cycle B has a higher proportion of it than does Cycle-A, indicating higher-energy depositional environments.

Komia boundstone is normally deposited at mound bumps. However, neither the Cycle A nor Cycle B has carbonate mound tops characterized by *Komia* boundstone. This is due to lack of core data containing this type of lithofacies. The Kirkland, I.E. #A-6, Eliasville Caddo #46, and Eliasville Caddo #106 well are the only three available wells having boundstone on their cores. The Arkins, A.A. #5 well, which is located at the thickest mound core, lacks the record of boundstones in its core. The absence of sufficient boundstone data makes it hard to conduct the lithofacies simulation and prediction.

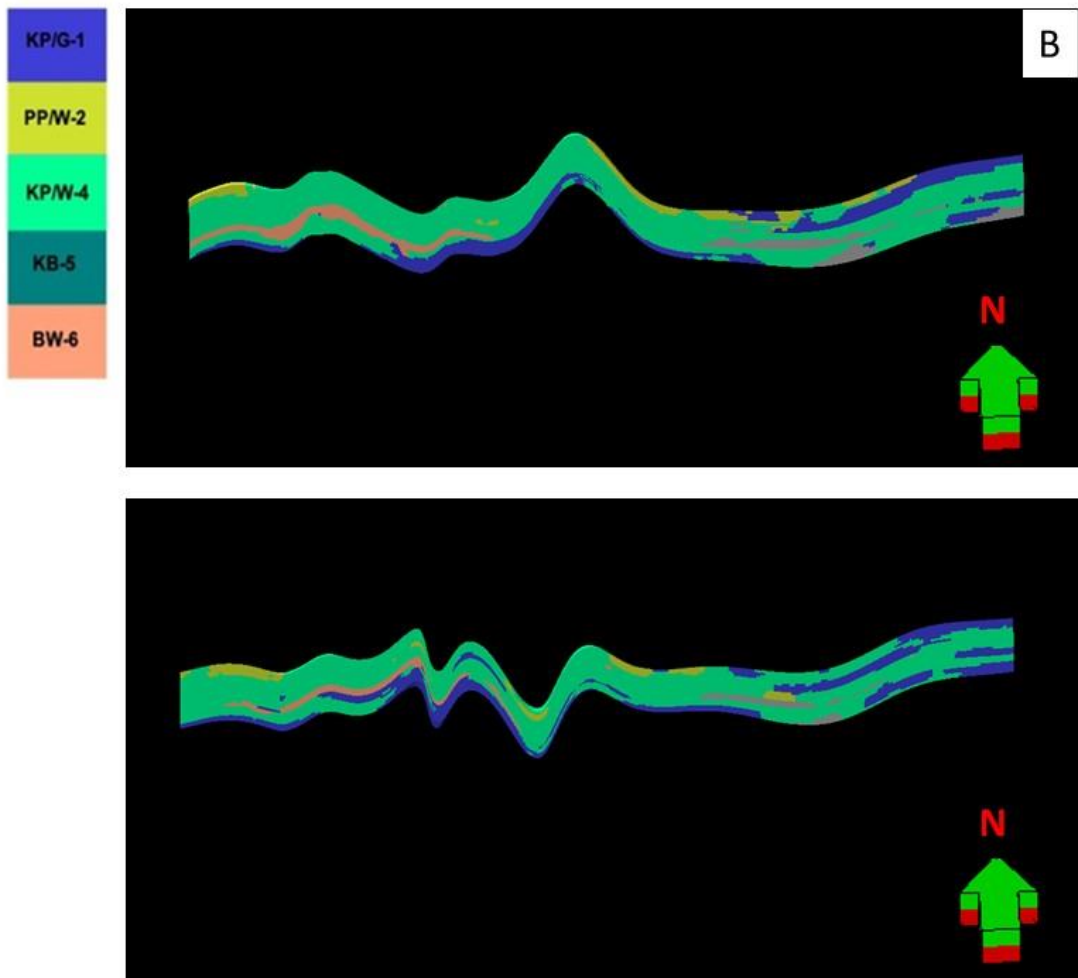
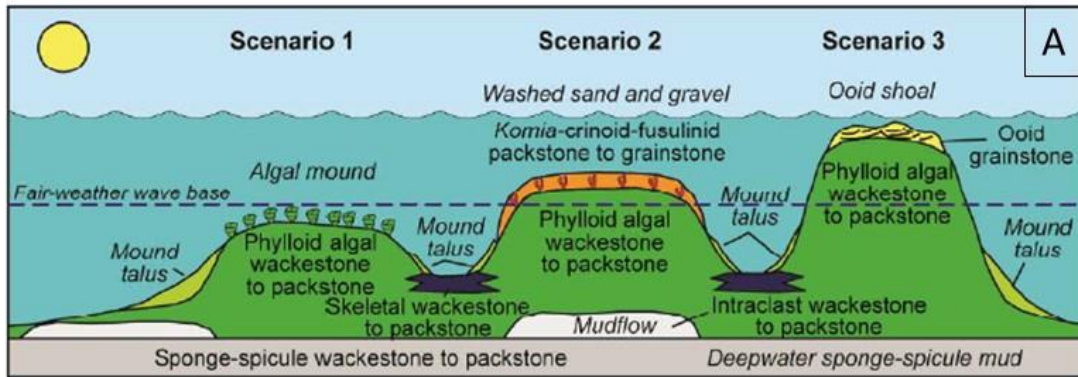


Figure 37. (A) Depositional model of Caddo mound complexes shows *Komia* flat formed above fair-weather wave base at the top of a phylloid algal mound, after Fu & Loucks, 2017. (B) Cross section of two carbonate mounds showing the vertical distribution of lithofacies at Cycle A.

By comparing the schematic graph and the model, some conclusions can be drawn about the evolution of carbonate mounds. When the mound was several meters below sea level, phylloid algae flourished and dominated the mound core (Figure 6-1-A) (Fu & Loucks, 2017). When relative sea level fell, phylloids algae at the mound crest were gradually replaced by *Komia*, which had a stronger habit and ability to thrive in higher wave energy. Thus the mound cores are dominated by *Komia*, the calcareous red algae. Phylloid algae occupy mound flanks, having sufficient sunlight and a lower energy level. Bioclast wackestone and packstone are mainly distributed at the inter-mound zones and at the bottom of carbonate mounds.

The modelling process provided a probability model of the lithofacies distributions. Unlike Adams (2005), this study of the Caddo Limestone did not have any outcrop data, making the final model potentially less precise. However, Adams (2005) utilized object modelling methods conditioned by two-dimensional outcrop-derived information. Janson and Madriz (2012) compared both multi-point statistics and sequential Gaussian simulation (SGS) with secondary trend data to model phylloid algal mounds. Multi-point statistics allowed them to reproduce the pattern in a training image, and required the dataset to be stationary. However, carbonate mounds are dynamic, making replicating the geological patterns more challenging. Multi-point statistics could reproduce the distribution of mound core versus flank but struggled with the regional variation. SGS incorporated vertical proportion curves and thickness trend map, but also had limitations (Janson and Madriz, 2012). Nonetheless, these methods could be utilized in modelling the Caddo Limestone to increase the model's integrity (Figure 6-1 (A)).

Galli (2006) adopted conventional object-based modelling techniques and pixel-based modelling algorithms. For TPG, Gaussian random functions were simulated first and the lithofacies type rule was applied. Galli (2006) demonstrated modelling reservoir architecture with truncated Pluri-Gaussian random functions in the Paradox Basin. The simulation showed a good outcome for the distribution of mound and

intermound facies. It also did well in the transitions between facies, which could vary with horizontal or vertical directions.

Comparatively, this study of the Caddo Limestone failed to characterize the intermounds accurately, or the smooth transition between different lithotypes. Some improvements could be made through having better data and algorithms. Both Galli (2006) and Janson and Madriz (2012) used outcrops as an important source of data for modelling. Further improvements on the modelling of the Caddo Limestone can be made with more outcrop data. Algorithm wise, all three studies applied a Gaussian algorithm instead of a Kriging algorithm, making the lithofacies and the transition of lithofacies more continuous and smooth.

One major defect of the artificial neural network approach is that thin beds smaller than 1 ft are hard to predict (Moinard, 1987). In light of this, major improvements can be achieved through making more accurate predictions of the depth of a lithofacies type, by increasing the number of iterations, and decreasing the error tolerance (Dedecker et al., 2004).

Lithofacies distribution maps are helpful for evaluations of reservoir quality. Cycle A is observed to be a good reservoir for hydrocarbons. According to results from thin sections, well-developed pore networks are composed of both macropores and micropores, and mainly occur in phylloid-algal lithofacies and *Komia* wackestone and packstone (Fu et al., 2017). The facies map indicates that phylloid-algal wackestone and packstone is mainly distributed throughout the Cycle-A. *Komia* wackestone and packstone is widespread across both cycles, however, the proportion of this lithofacies is higher in Cycle A. Therefore, Cycle A serves as a better hydrocarbon reservoirs. Further study might be focused on the reservoir property map, which can be constructed based on the lithofacies map with additional porosity and permeability data. The reservoir property model can be quantified on the basis of the lithofacies model (Huang et al., 1996).

Conclusion

The Concho Arch and the Bend Arch in the Concho Platform played a significant part in the development of the algal mounds. They influenced the mounds growing in approximately a northwest-southeast direction.

The carbonate reservoir of the Caddo Limestone shows much heterogeneity in its lithofacies distribution across the study area. Lithofacies vary rapidly vertically, from a scale of inches to feet. Based on gamma ray (GR) data, two cycles are defined at the uppermost interval of the Caddo Limestone: Cycle A at the top, and Cycle B beneath it. Based on the core description and thin section analysis, five lithofacies types are classified by Dunham's (1962) limestone classification criteria. These lithofacies are: (1) *Komia* wackestone and mud-dominated packstone, (2) phylloid-algal wackestone and packstone, (3) bioclast wackestone to packstone, (4) *Komia* grainstone and grain-dominated packstone, and (5) *Komia* boundstone. The internal architecture of the algal mounds can be observed from a three-dimensional lithofacies map. The *Komia* wackestone and mud-dominated packstone is widespread across Cycle A and Cycle B. It is especially abundant in Cycle A. Phylloid algae wackestone and packstone is distributed only in the uppermost of the Caddo Limestone at the lowest energy settings. Bioclast wackestone mainly accumulates at the inter-mound areas. From an energy point of view, the lithofacies distribution map is good evidence of a shallowing-upward sequence of the Caddo algal mounds, with the energy levels increasing upward.

From a modelling point of view, this facies distribution model still has some defects to be overcome. The main defect of the model is about *Komia* boundstone, which should have been taking place as the capping unit deposited at the mound bumps, yet due to the limitations of data,

it does not show up often. This problem can be solved with more data from core samples and by having improved algorithms. The more cored wells there are, the more accurate a probability model will be. Also, algorithms should be improved to become more sensitive to intervals of less than 1 ft so that small layers (<1 ft) from the core description will be simulated by the artificial neural network. Possible options might also be using multi-point statistics with a training image to construct a more accurate model for the intermound areas. Despite these defects, this model will still be helpful for locating hydrocarbon reserves. Major reserves are predicted to be in the uppermost part of the Caddo Limestone (Cycle A), where the phylloid-algal lithofacies and *Komia* lithofacies are the most abundant. Since other researchers have already tied porosity and permeability to certain lithofacies, reservoir-property maps of porosity and permeability distributions can be constructed with the help of lithofacies distribution maps.

References

- Abouelresh, M. O., & Slatt, R. M. (2012). Lithofacies and sequence stratigraphy of the Barnett Shale in east-central Fort Worth Basin, Texas. *Geohorizon*. AAPG Bulletin, 96(1), 1-22.
- Almazán-Vázquez, E., Buitrón-Sánchez, B. E., Vachard, D., Mendoza-Madera, C., & Gómez-Espinosa, C. (2007). The late Atokan (Moscovian, Pennsylvanian) chaetetid accumulations of Sierra Agua Verde, Sonora (NW Mexico): composition, facies and palaeoenvironmental signals. *Geological Society, London, Special Publications*, 275(1), 189-200.
- Brinton, L., & Wray, J. L. (1986). Pennsylvanian (Minturn Formation) Algal-Mound Facies, Rio Blanco, Colorado.
- Carr-Brown, B., 1973, The Holocene/Pleistocene contact in the offshore area east of Galeota Point, Trinidad, West Indies: IV Conferencia geologica del Caribe, Margarita, Venezuela, p. 381-397.
- Cheney, T.M., Sheldon, R.P., Cressman, E.R., Smart, R.A., and Carswell, L.K., 1953, Stratigraphic sections of the Phosphoria Formation measured and sampled in 1952: U.S. Geol. Survey open-file report.
- Chidsey Jr, T. C., Eby, D. E., & Lorenz, D. M. (1996). Geological and reservoir characterization of small shallow-shelf carbonate fields, southern Paradox Basin, Utah.
- Cleaves, A. W. (2000). Sequence stratigraphy and reciprocal sedimentation in Middle and Late Pennsylvanian carbonate-bank systems, Eastern shelf of the Midland Basin, north-central Texas. In *Platform carbonates in the southern mid-continent, 1996 symposium*: Norman, University of Oklahoma (Vol. 101, pp. 227-257).
- Colacicchi, R., & Baldanza, A. (1986). Carbonate turbidites in a Mesozoic pelagic basin: Scaglia Formation, Apennines—comparison with siliciclastic depositional models. *Sedimentary Geology*, 48(1-2), 81-105.
- Crabtree, J. L. (1987). Caddo Lime Reservoirs in the Bend Arch Area, North Central Texas. In *Southwest Section of AAPG Convention Transactions with Abstracts* (pp. 106-120). Dallas Geological Society.
- Cross, T. A., & Klosterman, M. J. (1981). Autecology and development of a stromatolitic-bound phylloid algal bioherm, Laborcita Formation (Lower Permian), Sacramento Mountains, New Mexico, USA. In *Phanerozoic Stromatolites* (pp. 45-59). Springer, Berlin, Heidelberg.
- Day-Stirrat, R. J., Loucks, R. G., Milliken, K. L., Hillier, S., & van der Pluijm, B. A. (2008). Phyllosilicate orientation demonstrates early timing of compactional stabilization in calcite-

- cemented concretions in the Barnett Shale (Late Mississippian), Fort Worth Basin, Texas (USA). *Sedimentary Geology*, 208(1-2), 27-35.
- Day-Stirrat, R. J., Loucks, R. G., Milliken, K. L., Hillier, S., & van der Pluijm, B. A. (2008). Phyllosilicate orientation demonstrates early timing of compactional stabilization in calcite-cemented concretions in the Barnett Shale (Late Mississippian), Fort Worth Basin, Texas (USA). *Sedimentary Geology*, 208(1-2), 27-35.
- Dedecker, A. P., Goethals, P. L., Gabriels, W., & De Pauw, N. (2004). Optimization of Artificial Neural Network (ANN) model design for prediction of macroinvertebrates in the Zwalm river basin (Flanders, Belgium). *Ecological Modelling*, 174(1-2), 161-173.
- Dihlberg, E. E. (1989). Brachiopod Biostratigraphy and Biofacies Analysis of the Marble Falls Formation (Pennsylvanian) of Central Texas.
- Dunham, R. J. (1962). Classification of carbonate rocks according to depositional textures.
- Entzminger, D. J., Canter, L., Sonnenfeld, M., & Gardner, S. Waterflooding the Parks (Caddo) Field, Stephens County, Texas.
- Föllmi, K. B. (1995). 160 my record of marine sedimentary phosphorus burial: Coupling of climate and continental weathering under greenhouse and icehouse conditions. *Geology*, 23(6), 503-506.
- Forehand, M. T. (1991). Deposition and diagenesis of Caddo mud mounds, in the Breckenridge field, Stephens County, Texas. The University of Texas at Arlington.
- Freeman, T. (1964). Algal limestones of the Marble Falls Formation (Lower Pennsylvanian), Central Texas. *Geological Society of America Bulletin*, 75(7), 669-676.
- Fu, Q., Ambrose, W. A., & Barton, J. W. (2017). Reservoir characterization of the Pennsylvanian Caddo Limestone in Stephens County, Texas: A case study of Komia-dominated algal mounds. *Marine and Petroleum Geology*, 86, 991-1013.
- Gardner, M. W., & Dorling, S. R. (1998). Artificial neural networks (the multilayer perceptron)—a review of applications in the atmospheric sciences. *Atmospheric environment*, 32(14-15), 2627-2636.
- Goh, A. T. (1995). Back-propagation neural networks for modeling complex systems. *Artificial Intelligence in Engineering*, 9(3), 143-151.
- Grammar, G. M., & Eberli, G. P. (1998). Exploration and Production Scale Lateral Variability in Phylloid Algal Mound and Associated Reservoir Facies, Paradox Basin, SE Utah. *PUBLICATIONS-WEST TEXAS GEOLOGICAL SOCIETY*, 139-152.

- Grayson, R. C., Merrill, G. K., Lambert, L. L., Trice III, E. L., Vitani, N. M., & Westergaard, E. H. (1987). Middle Pennsylvanian strata of central Texas: Stratigraphic and conodont biostratigraphic relationships. Early and Late Paleozoic conodont faunas of the Llano Uplift region, central Texas: Biostratigraphy, systemic boundary relationships and stratigraphic importance Guidebook for Field Trip, 1(1987), 73-82.
- Hart, B. S., Longstaffe, F. J., & Plint, A. G. (1992). Evidence for relative sea level change from isotopic and elemental composition of siderite in the Cardium Formation, Rocky Mountain Foothills. *Bulletin of Canadian Petroleum Geology*, 40(1), 52-59.
- Hecht-Nielsen, R. (1992). Theory of the backpropagation neural network. In *Neural networks for perception* (pp. 65-93).
- Heckel, P. H. (1974). Carbonate buildups in the geologic record: a review.
- Heckel, P. H., & Cocke, J. M. (1969). Phylloid algal-mound complexes in outcropping Upper Pennsylvanian rocks of Mid-Continent. *AAPG Bulletin*, 53(5), 1058-1074.
- Hentz, T. F., Ambrose, W. A., & Carr, D. L. (2012). Reservoir systems of the Pennsylvanian lower Atoka Group (Bend Conglomerate), northern Fort Worth Basin, Texas: High-resolution facies distribution, structural controls on sedimentation, and production trends Reservoir Systems of the Lower Atoka Group, Northern Fort Worth Basin. *AAPG Bulletin*, 96(7), 1301-1332.
- Huang, Z., Shimeld, J., Williamson, M., & Katsube, J. (1996). Permeability prediction with artificial neural network modeling in the Venture gas field, offshore eastern Canada. *Geophysics*, 61(2), 422-436.
- Janson, X., & Madriz, D. D. (2012). Geomodelling of carbonate mounds using two-point and multipoint statistics. *Geological Society, London, Special Publications*, 370, SP370-5.
- Jarvie, D. M., Hill, R. J., Ruble, T. E., & Pollastro, R. M. (2007). Unconventional shale-gas systems: The Mississippian Barnett Shale of north-central Texas as one model for thermogenic shale-gas assessment. *AAPG bulletin*, 91(4), 475-499.
- Jung, A., & Aigner, T. (2012). Carbonate geobodies: Hierarchical classification and database—a new workflow for 3D reservoir modelling. *Journal of Petroleum Geology*, 35(1), 49-65.
- Kenter, J. A., Van Hoeflaken, F., Bahamonde, J. R., Gartner, G. L. B., Keim, L., & Besems, R. E. (2002). Anatomy and lithofacies of an intact and seismic-scale Carboniferous carbonate platform (Asturias, NW Spain): analogs of hydrocarbon reservoirs in the Pricaspian basin (Kazakhstan).
- Khawiwada, M., Keller, G. R., & Marfurt, K. J. (2013). A window into the Proterozoic: Integrating 3D seismic, gravity, and magnetic data to image subbasement structures in the southeast Fort Worth basin A window into the Proterozoic. *Interpretation*, 1(2), T125-T141.

- Kier, R. S., Brown, L. F., & McBride, E. F. (1980). The Mississippian and Pennsylvanian (Carboniferous) Systems in the United States--Texas. Bureau of Economic Geology, University of Texas at Austin.
- Lewis, E. G. (1987). A Microfacies/Seismic Interpretation of the Caddo Lime in the Chalky Mountain Field of Northwest Taylor County, Texas. In Southwest Section of AAPG-1987 Convention Transactions with Abstracts (pp. 130-143).
- Loucks, R. G., & Fu, Q. (2016). Origin and Characterization of the Lithofacies and Dual Micropore/Macropore Network in Pennsylvanian (Early Desmoinesian) Caddo Shelf-Buildup Complexes, Stephens County, North-Central Texas.
- Lucia, F. J. (2007). Carbonate reservoir characterization: An integrated approach. Springer Science & Business Media.
- Loucks, R. G., & Ruppel, S. C. (2007). Mississippian Barnett Shale: Lithofacies and depositional setting of a deep-water shale-gas succession in the Fort Worth Basin, Texas. AAPG bulletin, 91(4), 579-601.
- Melnyk, D. H., & Maddocks, R. F. (1988). Ostracode biostratigraphy of the Permo-Carboniferous of central and north-central Texas, Part I: paleoenvironmental framework. *Micropaleontology*, 1-20.
- Merrill, M. D., Slucher, E. R., Roberts-Ashby, T. L., Warwick, P. D., Blondes, M. S., Freeman, P. A., ... & Lohr, C. D. (2012). Geologic Framework for the National Assessment of Carbon Dioxide Storage Resources: Permian and Palo Duro Basins and Bend Arch-Fort Worth Basin. U.S. Department of the Interior, U.S. Geological Survey.
- Miller, M. C. (2001). Petrographical, petrophysical, and biostratigraphical investigation of the Caddo Limestone (Pennsylvanian) Stephens County, Texas (Doctoral dissertation, Texas Tech University).
- Moinard, L. (1987). Application of Kriging to the mapping of a reef from wireline logs and seismic data; a case history. In *Geostatistical Case Studies* (pp. 93-103). Springer, Dordrecht.
- Montgomery, S. L., Jarvie, D. M., Bowker, K. A., & Pollastro, R. M. (2005). Mississippian Barnett Shale, Fort Worth basin, north-central Texas: Gas-shale play with multi-trillion cubic foot potential. AAPG bulletin, 89(2), 155-175.
- Nakazawa, T., Ueno, K., & Wang, X. (2009). Sedimentary facies of Carboniferous-Permian mid-oceanic carbonates in the Changning-Menglian Belt, West Yunnan, Southwest China: Origin and depositional process. *Island Arc*, 18(1), 94-107.

- Olden, J. D., & Jackson, D. A. (2002). Illuminating the “black box”: a randomization approach for understanding variable contributions in artificial neural networks. *Ecological modelling*, 154(1-2), 135-150.
- Pollastro, R. M. (2007). Total petroleum system assessment of undiscovered resources in the giant Barnett Shale continuous (unconventional) gas accumulation, Fort Worth Basin, Texas. *AAPG bulletin*, 91(4), 551-578.
- Pollastro, R. M., Jarvie, D. M., Hill, R. J., & Adams, C. W. (2007). Geologic framework of the Mississippian Barnett shale, Barnett-paleozoic total petroleum system, Bend arch–Fort Worth basin, Texas. *AAPG bulletin*, 91(4), 405-436.
- Pradhan, B., & Lee, S. (2010). Landslide susceptibility assessment and factor effect analysis: backpropagation artificial neural networks and their comparison with frequency ratio and bivariate logistic regression modelling. *Environmental Modelling & Software*, 25(6), 747-759.
- Qi, L., & Carr, T. R. (2006). Neural network prediction of carbonate lithofacies from well logs, Big Bow and Sand Arroyo Creek fields, Southwest Kansas. *Computers & Geosciences*, 32(7), 947-964.
- Riedmiller, M. (1994). Advanced supervised learning in multi-layer perceptrons—from backpropagation to adaptive learning algorithms. *Computer standards and interfaces*, 16(3), 265-278.
- Ritter, S. M., Barrick, J. E., & Skinner, M. R. (2002). Conodont sequence biostratigraphy of the Hermosa Group (Pennsylvanian) at Honaker Trail, Paradox Basin, Utah. *Journal of Paleontology*, 76(3), 495-517.
- Ross, C.A., and Ross, J.R.P., 1987, Late Paleozoic sea levels and depositional sequences, in Ross, C.A., and Haman, D., eds., *Timing and depositional history of eustatic sequences: Constraints on seismic stratigraphy: Cushman Foundation for Foraminiferal Research Special Publication 24*, p. 137-149.
- Saller, A. H., Dickson, J. A. D., & Matsuda, F. (1999). Evolution and distribution of porosity associated with subaerial exposure in upper Paleozoic platform limestones, west Texas. *AAPG bulletin*, 83(11), 1835-1854.
- Saller, A. H., Dickson, J. A. D., Rasbury, E. T., & Ebato, T. (1999b). Effects of long-term accommodation change on short-term cycles, upper Paleozoic platform limestones, west Texas.
- Samankassou, E., & West, R. R. (2002). Construction versus accumulation in phylloid algal mounds: an example of a small constructed mound in the Pennsylvanian of Kansas, USA. *Palaeogeography, Palaeoclimatology, Palaeoecology*, 185(3-4), 379-389.

- Tinker, S. W., Caldwell, D. H., Cox, D. M., Zahm, L. C., & Brinton, L. (2004). Integrated reservoir characterization of a carbonate ramp reservoir, South Dagger Draw field, New Mexico: Seismic data are only part of the story.
- Tang, H., Meddaugh, W. S., & Toomey, N. (2011). Using an artificial-neural-network method to predict carbonate well log facies successfully. *SPE Reservoir Evaluation & Engineering*, 14(01), 35-44.
- Toomey, D. F., & Winland, H. D. (1973). Rock and biotic facies associated with Middle Pennsylvanian (Desmoinesian) algal buildup, Nena Lucia Field, Nolan County, Texas. *AAPG Bulletin*, 57(6), 1053-1074.
- Turner, G.L. 1957, Paleozoic Stratigraphy of the Fort Worth basin: Abilene and Fort Worth Geol. Socs. Joint Field Trip Guidebook, p. 57-77.
- Van Wagoner, J. C. (1977). Lower and middle Pennsylvanian Rocks of the Norther Sacramento Mountains: A Study of Contemporaneous Carbonate and Siliciclastic Deposition in an Active Tectonic Setting (NEW MEXICO) (Doctoral dissertation, Rice University).
- Wahlman, G. P. (1985). Lower Permian (Wolfcampian) Archaeolithoporella-Tubiphytes-sponge boundstones from the subsurface of west Texas. In *Paleoalgology* (pp. 208-215). Springer, Berlin, Heidelberg.
- Weber, L. J. (1995). Depositional and diagenetic control of reservoir quality and continuity of the Pennsylvanian Caddo Limestone. *Carbonate Facies and Sequence Stratigraphy: Practical Applications of Carbonate Models, SEPM*, 257-286.
- Weber, L. J., Sarg, J. R., & Wright, F. M. (1995). Sequence stratigraphy and reservoir delineation of the middle Pennsylvanian (Desmoinesian), Paradox Basin and Aneth field, southwestern USA.
- Yancey, T. E., & Cleaves, A. W. (1990). Carbonate and Siliciclastic Sedimentation in Late Pennsylvanian Cycles, North-Central Texas.
- Yose, L. A., Ruf, A. S., Strohmenger, C. J., Schuelke, J. S., Gombos, A., Al-Hosani, I., ... & Johnson, I. G. (2006). Three-dimensional characterization of a heterogeneous carbonate reservoir, Lower Cretaceous, Abu Dhabi (United Arab Emirates).

Vita

Wentao (“Tom”) Wang was born in Dongying, Shandong Province and raised in Beijing, China. Wentao graduated from The High School Affiliated to Renmin University of China with an extraordinary record in National College Entrance Examination (Science) and from The University of Hong Kong with a bachelor of Electronic Engineering. In September 2016, he enrolled in the Jackson School of Geosciences at The University of Texas at Austin, where his research interest was carbonate reservoir modelling. After receiving his Master’s in Geosciences from UT-Austin, he will be working as an energy consultant for Wood Mackenzie, at Houston, Texas.

Email: wentao.austin@gmail.com

This thesis was typed by the author, Wentao Wang.